LA-UR-19-25177
Approved for public release; distribution is unlimited.

Title: An eddy-permitting ocean-sea ice general circulation model (E3SMv0-HiLAT03): Description and evaluation

Author(s): Zhang, Jiaxu
Weijer, Wilbert
Maltrud, Mathew Einar
Veneziani, Carmela
Jeffery, Nicole
Hunke, Elizabeth Clare
Urrego Blanco, Jorge Rolando
Wolfe, Jonathan David

Intended for: Report

Issued: 2019-07-12 (rev.2)

An eddy-permitting ocean-sea ice general circulation model (E3SMv0-HiLAT03): Description and evaluation

Jiaxu Zhang[1,2], Wilbert Weijer[1], Mathew E. Maltrud[3], Milena Veneziani[3], Nicole Jeffery[1], Elizabeth C. Hunke[3], Jorge R. Urrego-Blanco[1], and Jonathan D. Wolfe[3]

[1] *Computational Physics and Methods (CCS-2), Los Alamos National Laboratory, Los Alamos, NM.*

[2] *Center for Nonlinear Studies (CNLS), Los Alamos National Laboratory, Los Alamos, NM.*

[3] *Fluid Dynamics and Solid Mechanics (T-3), Los Alamos National Laboratory, Los Alamos, NM.*

June 20, 2019

Los Alamos Technical Report

(LA-UR-19-25177)

Abstract

We document modeling setups and present results for simulated ocean and sea ice climate from a recently developed, intermediate-resolution global ocean-sea ice model [Energy Exascale Earth System Model version 0 configured for High-Latitude Application and Testing at 0.3° resolution (E3SMv0-HiLAT03)]. The horizontal resolution of HiLAT03 ranges from 33 km in the tropics to 8.5 km at high latitudes, with 100 vertical levels. This resolution allows the explicit representation of some mesoscale eddies, particularly at lower latitudes, therefore being named as an "eddy-permitting model". Analyses are presented based on the output of two 186-yr control simulations forced by modern atmospheric conditions of climatological and inter-annually varying data sets, respectively. Results are compared to available observational data sets and the 1° NCAR model, which has somewhat similar ocean physics but a coarser resolution and an earlier version of the sea ice component. Analyses focus on ocean temperature and salinity fields, ocean dynamics and circulations, sea ice concentrations and thicknesses. The HiLAT03 model does reasonably well in most oceanic aspects evaluated here, especially in ocean meridional heat transport, despite the fact that no explicit eddy parameterization is applied. Many Arctic sea ice features are much improved compared with the 1° NCAR model, but the Antarctic summer sea ice is still generally low in concentrations and thicknesses. In addition, we discuss the prolonged deep convection ("Antarctic prolonged polynya") over the Southern Ocean in the inter-annually forced case.

1 Introduction

The purpose of this report is to document the parameterization setups of the ocean and sea ice components of the E3SMv0-HiLAT climate model in the 0.3° horizontal resolution configuration (hereafter referred to as HiLAT03), and provide a general overview of the salient features of the ocean and sea ice climate in two control simulations forced by present-day atmospheric conditions.

Ocean mesoscale eddies play an important role in the dynamics of the major ocean current systems, such as the Antarctic Circumpolar Current (ACC) and the western boundary currents (e.g., Kuroshio, Gulf Stream) (*Hecht and Hasumi*, 2008; *Waterman et al.*, 2011). The spatial scales of mesoscale eddies are generally characterized by the first baroclinic Rossby radius of deformation, which is defined as $L = \sqrt{c_g^2/(f^2 + 2\beta c_g)}$, where c_g is the first-mode internal gravity wave speed, f is the Coriolis parameter, and $\beta = \partial f/\partial y$ is its meridional gradient. The Rossby radius varies with latitude and ocean bathymetry, and is in general large in low latitudes and open oceans and small in high latitudes and coastal areas. The ocean components of the current generation of models for climate prediction are typically configured at 1° resolution (e.g., CMIP6 climate models; *Eyring et al.*, 2016), which can explicitly represent eddies only within a narrow band along the equator. In order to replicate the dynamics of the real ocean, they need a suitable parameterization to represent

these eddy activities, such as the *Gent and Mcwilliams* (1990) parameterization (GM parameterization). But any such parameterization is associated with uncertain assumptions about the properties of the eddies and may lead to suppressed eddy kinetic energy and weak eddy-induced transport. High resolution models at 0.1° or even finer configurations, on the other hand, explicitly resolve mesoscale eddies in much of the ocean from 60°S to 60°N (*Hallberg*, 2013), but they are too computationally expensive to support global scale, long-term climate simulations. Regional models are increasingly being used for climate studies at resolutions of several kilometers, such as the Regional Arctic System Model (*Maslowski et al.*, 2012), which has an ocean and sea-ice resolution of 1/12°. Such regional models are suitable for exploring local, small-scale processes (*Roberts et al.*, 2015; *Cassano et al.*, 2017), but cannot be used to estimate remote, large-scale climatic impacts.

An intermediate resolution model ranging from 0.5° to 0.25°, also known as "eddy-permitting" configuration, is a reasonable compromise, as it allows for explicitly resolving eddy activity in larger parts of the ocean than the 1° models, while keeping the flexibility of both short-term and long-term simulations. A good handful of eddy-permitting ocean models, either stand-alone (*Liu et al.*, 2004; *Madec and the NEMO Team*, 2016; *Maltrud and Holloway*, 2008) or coupled to other Earth system components (*Williams et al.*, 2015; *Delworth et al.*, 2012; *Rothstein et al.*, 2006), have been developed in the past two decades and have been applied to global scale, ocean circulation topics, such as the Atlantic Meridional Overturning Circulation (AMOC) (*Spence et al.*, 2008; *Gary et al.*, 2011; *Mecking et al.*, 2017, 2016). We expect many IPCC-class ocean models will feature eddy-permitting configurations in the near future (*Jansen et al.*, 2015).

The eddy-permitting resolutions produce eddy-like disturbances generated by ocean baroclinic instability, but are still insufficiently refined to properly resolve the mesoscale eddy field, especially at mid to high latitudes or on the continental shelves (*Hallberg*, 2013). It remains an issue of how to deal with the effect of mesoscale eddies in regions where these eddies are not or only partly represented (*Fox-Kemper and Menemenlis*, 2008). Some models choose not to include a mesoscale eddy parameterization in tracer transport equations (e.g., GFDL CM2.5; *Delworth et al.*, 2012), while others use an original or modified GM-parameterization globally (e.g., NEMO ORCA025; *Madec and the NEMO Team*, 2016). Though advanced schemes have been proposed, such as using a resolution function to regulate parameterization (*Hallberg*, 2013) or adding a backscatter term to counteract the energy dissipation of hyperviscous closures (*Jansen et al.*, 2015), they have only been tested in idealized models and have not yet been widely adopted by ocean general circulation models (GCMs). In this particular version of the ocean model, HiLAT03 can explicitly represent eddies within the 20°S–20°N band. We choose not to include a mesoscale eddy parameterization in this model, mostly to facilitate an assessment of the role of oceanic eddies in the ocean system. We will focus the model evaluation on ocean energy and tracer transport under this choice.

This report is organized as follows. A description of the model components and specific 0.3° configuration experiments is presented in Section 2. Section 3 presents the model's ocean climatology, featuring the temperature and salinity fields, the ocean general circulation and

transports, and an Antarctic prolonged polynya which occurs in the inter-annually forced control simulation. Section 4 presents the model's sea ice climatology, with a focus on the sea ice extent and volume. Conclusions and discussions are made in Section 5.

2 Model and Experiments

The ocean-sea ice GCM documented in this report is a 0.3° configuration (tx0.3v2) of the E3SMv0-HiLAT model code. E3SMv0-HiLAT (*Hecht et al.*, 2019b) is a fully-coupled Earth System Model (ESM) based on the Community Earth System Model version 1 (CESM1) (*Hurrell et al.*, 2013), with development priorities focusing on improved representation of the high latitude Earth system. The ocean component of E3SMv0-HiLAT uses the Parallel Ocean Program version 2 (POP2) (*Smith et al.*, 2010), which is essentially the same as that is used in CESM1; while its sea ice component uses the Los Alamos Sea Ice Model version 5 (CICE5) (*Hunke et al.*, 2015), an updated version of CICE4 that is used in CESM1.

2.1 The HiLAT03 POP2 ocean model

The HiLAT03 configuration of POP2 has a horizontal grid with nominal resolution of 0.3°, ranging from 33 km in the tropics to 8.5 km at high latitudes. It has a tripole layout with two northern poles in Canada and Russia (*Murray*, 1996), which avoids placing a physical boundary or grid singularity in the Arctic Ocean. Compared with the dipole grid that is used in the 1° configuration of this model (gx1v6), the tripole grid has a much more uniform grid spacing in the Arctic and the cell aspect ratios are much closer to 1. This 0.3° mesh is a subsampled version of the 0.1° mesh used in many other studies, such as the ocean-only simulation (*Weijer et al.*, 2012), the E3SMv0 high-resolution (E3SMv0-HR) simulations (*Kurtakoti et al.*, 2018), and the CESM Accelerated Scientific Discovery (ASD) simulation (*Small et al.*, 2014).

The number of vertical levels has been increased from 60 levels in gx1v6 to 100 in this version, ranging in thickness from 6 m to 150 m, with the first layer centered at 3 m and the bottom layer centered at 5925 m. The vertical levels have been increased in order to better resolve upper ocean processes, from polar stratification to mixed layer depths, the vertical temperature structures, and biogeochemical dynamics. The bottom topography is discretized as partial bottom cells (*Adcroft et al.*, 1997) to allow a more accurate representation of topographic slopes than the traditional full-cell approach.

As explained in the introduction section, neither the horizontal mesoscale eddy parameterization nor the submesoscale mixed-layer parameterization, which are used in gx1v6, is included in the present version. Tracer advection uses a one-dimensional flux-limited version of the second-order Lax-Wendroff algorithm (*Smith et al.*, 2010), which is designed to reduce, but not completely eliminate, the production and amplification of artificial extrema. In comparison, gx1v6 uses third-order upwind advection (*Leonard*, 1979). The reason why

we use this advection scheme instead of others available in POP2 (centered or third-order upwind) is that this is the only scheme that does not require explicit diffusion to prevent the generation of false extrema.

The HiLAT03 configuration uses biharmonic horizontal momentum mixing. The biharmonic viscosity coefficient is spatially varying, ranging from $A_M^4 = -8.1 \times 10^{18}$ at the equator to $A_M^4 = -0.14 \times 10^{18}$ at polar regions, and is negative for positive-definite dissipation of kinetic energy. In comparison, gx1v6 uses an anisotropic horizontal viscosity (*Large et al.*, 2001). The vertical mixing is modeled by the K-profile parameterization (KPP) (*Large et al.*, 1994), with the background vertical tracer diffusivity coefficient (κ) being depth dependent, ranging from 0.1 at the surface to 1.0 at the bottom.

Overflow parameterization, which has been implemented in POP2 for low resolution configurations to represent exchanges through narrow straits and channels and associated entrainment (*Yeager and Danabasoglu*, 2012), has been turned off in this version. We chose not to use it due to time/computational constraints, since such parameterization is grid specific (focused on a few specific locations) and iteratively tuned. Although the increased horizontal resolution (from 1° to 0.3°) and especially the increased vertical resolution (from 60 levels to 100 levels) allow the model to represent the overflow physics to some extent, the model is still a vertically z-coordinate model, which has staircase-like topography and tends to produce deep waters that are too light and remain too shallow without such a parameterization.

Another important update is the use of a local sea surface salinity (SSS) instead of the reference salinity in the virtual salt flux (VSF) formulation with regard to the river outflows. POP2 fixes the global integral of the ocean volume by converting the freshwater fluxes to VSF using a constant reference salinity of 34.7 psu. Though this ensures that the global freshwater and salt contents remain balanced, the calculated SSS can be unrealistic and even become negative, when the local SSS is much lower than the reference salinity in regions where large amounts of freshwater are discharged into the ocean (e.g., river outflows and sea ice melts). This problem becomes particularly evident in Arctic estuaries that have limited exchange with the open ocean, leading to salinities of -50 psu. To remedy this, we now use the local SSS in the VSF calculation for runoff to assure that no more salt can be extracted than what is available. We also apply this approach to meltwater fluxes due to sea ice melt, but note that this is leads to an inconsistency with the formulation of frazil ice formation, which still uses the constant reference salinity. Any imbalances in the salt budget due to non-zero net surface fluxes are remedied by scaling precipitation with a scaling factor that compensates for net salt content changes during the previous year. This precipitation factor is typically within a few percent of 1.

The information of model setup discussed here is summarized in Table 1, with a comparison to the default setup for the 1° NCAR model.

Table 1: Summary of the model setups for HiLAT03, with a comparison to the 1° POP2. The table includes horizontal and vertical resolution, the number of grid cells, advection, horizontal and vertical mixing, overflow parameterization, and changes made to virtual salt flux. Detailed descriptions can be found in the text.

	Dipole 1° global configuration (gx1v6)	Tripole 0.3° global configuration (tx0.3v2)
Resolution	1° lat×1° lon×60 level	0.3° lat×0.3° lon×100 level
Number of cells	$384 \times 320 \times 60$	$1200 \times 800 \times 100$
Advection	3rd order upwind	Flux-limited Lax-Wendroff
Horizontal diffusion	Gent-McWilliams and sub-mesoscale	No explicit parameterization
Horizontal viscosity	Anisotropic	Biharmonic
Vertical mixing	KPP	KPP
Overflow parameterization	On	Off
Virtual salt flux	Using global reference salinity	Using local surface salinity to runoff (ROFF_F) and sea ice melt (MELT_F)

2.2 The HiLAT03 CICE5 sea ice model

CICE5 solves dynamic and thermodynamic equations for multiple ice thickness categories in each horizontal grid cell (*Hunke et al.*, 2015). Version 5 has several new developments, the most significant being a mushy layer thermodynamics routine (*Turner and Hunke*, 2015) which solves prognostic equations for both ice enthalpy and salinity. Previous model versions assumed a fixed vertical salinity profile typical of multi-year ice but that underestimates salt content for first year ice. Resulting polar ice packs tend to be thicker with the new scheme, particularly in the Northern hemisphere. In addition, version 5 uses the level-ice melt pond parameterization (*Hunke et al.*, 2013) which includes a more physically based progression of pond area and spatial extent. The scheme stores and drains meltwater in level-ice basins, refreezes ponds, and allows snowfall to cover refrozen surfaces blocking penetrating radiation. In addition to thermodynamics, CICE computes the ice state evolution due to several key processes: 1) ice dynamics which evolves the ice velocity field assuming an elastic-viscous-plastic (EVP) rheology (*Hunke and Dukowicz*, 1997); 2) an incremental remapping transport code which describes advection of ice concentration, volume, tracers, and other state variables; and 3) a ridging parameterization which transfers ice between sub grid thickness categories.

The HiLAT03 configuration of CICE5 has the same horizontal grids as used in the ocean model. Many new parameterizations have been added or updated in CICE5 compared with CICE4 that is used in CESM, and their combinations have been tested (*Urrego-Blanco et al.*, 2016, 2017). The optimal choices for E3SMv0-HiLAT are documented in Table 1 of *Hecht et al.* (2019b).

2.3 Simulations

The atmospheric data set that is used to force our ocean-sea ice model is the Coordinated Ocean-Ice Reference Experiments version 2 (CORE-II; *Large and Yeager*, 2009; *Griffies et al.*, 2012), which has been a widely used framework to force ocean and/or sea ice models for hindcast simulations. The CORE-II data set is also used by the Coupled Model Intercomparison Project (CMIP) to evaluate ocean-sea ice models in many aspects such as the North Atlantic inter-annual to decadal variability (*Danabasoglu et al.*, 2016), Arctic sea ice and liquid freshwater (*Wang et al.*, 2016b,a), and Southern Ocean water masses and sea ice (*Downes et al.*, 2015), therefore allowing the assessment of our model performance in the context of other CMIP models. We performed two simulations, with one (GNYF hereafter) forced by the climatology (the so-called normal year forcing) and the other (GIAF hereafter) forced by the inter-annually varying data of the 62-year period from 1948 to 2009. We generated mapping files to map the CORE-II atmospheric and riverine data to the tx0.3v2 grid, respectively. When mapping the riverine data, we applied a Gaussian smoothing function with an exponential decay scale of 1000 km over a horizontal radius of 300 km for ocean areas near the river mouths.

Both simulations were initialized from the Polar Science Center Hydrographic Climatology (PHC2), which represents a blending of the *Levitus et al.* (1998) with *Steele et al.* (2001) data for the Arctic Ocean. We performed both simulations for 186 years, corresponding to three inter-annual forcing cycles. In both cases, a weak restoring term is included to maintain SSS close to observations, with a restoring time scale of 4 years over open ocean. During the course of the simulations a replacement of the data set that is used for surface salinity restoring was made. Starting from Year 54 of GNYF and Year 71 of GIAF, the PHC2 data is replaced by the World Ocean Atlas 2013 version 2 (WOA13v2; *Boyer et al.*, 2013), which represents salinity with more detail and less uncertainty due to large increases in the amount of data that is represented and better temporal and spatial coverage coupled with refined analysis and quality control techniques.

During the course of GIAF, a large sea ice opening associated with intense deep convection in the Southern Ocean formed and decayed in each forcing cycle, similar to open ocean polynyas but occurring over a prolonged period and extending over a much larger area. Details of this phenomenon will be discussed in Section 3.3. In order to investigate the sensitivity of this prolonged polynya to salinity restoring boundary condition, we performed a test (GIAF_SR hereafter) where SSS is not just restored in ice-free regions, but also under sea ice with the same intensity as in the ice-free regions.

3 Model Ocean Climatology

3.1 Temperature and salinity fields

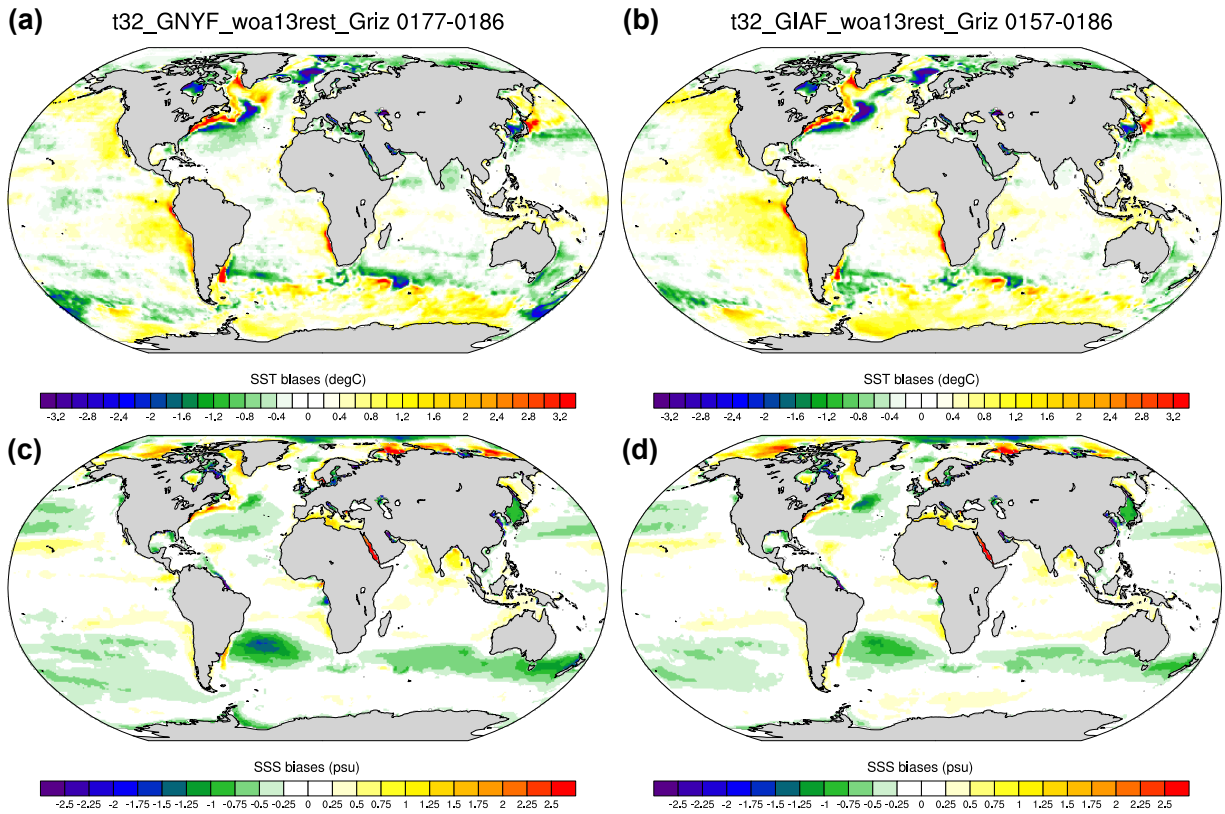

Figure 1: Climatological mean **(a, b)** sea surface temperature (SST) and **(c, d)** sea surface salinity (SSS) biases against WOA13v2 (*Boyer et al.*, 2013) for (left) GNYF and (right) GIAF.

Sea surface temperature and salinity patterns. The maps of the climatological mean sea surface temperature (SST) and SSS biases relative to the WOA13v2 data set (*Boyer et al.*, 2013) are shown in Figure 1. The global mean SST biases are +0.07°C and +0.20°C in GNYF and GIAF, respectively. The GNYF case produces similar global-mean SST biases compared with previous 1° POP2 (+0.06°C, *Danabasoglu et al.*, 2012), but the biases in GIAF is higher. The higher biases in GIAF are found in East Pacific, as well as in the Southern Ocean (Fig. 1b). One noticeable improvement in HiLAT03 is found in the subpolar North Atlantic, which used to show strong warm bias in coupled CCSM4 and forced 1° POP2 (*Danabasoglu et al.*, 2012). But in general, the overall SST biases are small compared with other coupled models (*Danabasoglu et al.*, 2012; *Griffies et al.*, 2015), indicating that the biases would be much reduced once the ocean model is forced by the best estimates of the atmospheric states. Chronic biases over coastal regions in previous POP2 versions (*Danabasoglu et al.*, 2012), such as the west coast of South America and Africa, are still obvious in HiLAT03, although improvements are found over the west coast of North America and tropical Africa.

HiLAT03 exhibits a mild, overall fresh SSS bias, with the global-mean value of −0.08 psu in GNYF and −0.02 psu in GIAF (Fig. 1c and d). In comparison, the 1° POP2 shows a salty bias of +0.06 psu (*Danabasoglu et al.*, 2012). The most noticeable improvements are in the tropical regions, which used to show strong salty bias in the 1° POP2, largely

because of the improved tropical ocean dynamics due to the increased resolution, as well as the use of a local SSS instead of the reference salinity in the VSF formulation. Major rivers with large discharge rates, such as the Amazon, Congo, and Ganges Rivers, outflow to the tropical ocean. Using the local SSS instead of a much higher reference salinity in the VSF formulation over the outflow regions strongly corrects the salty biases.

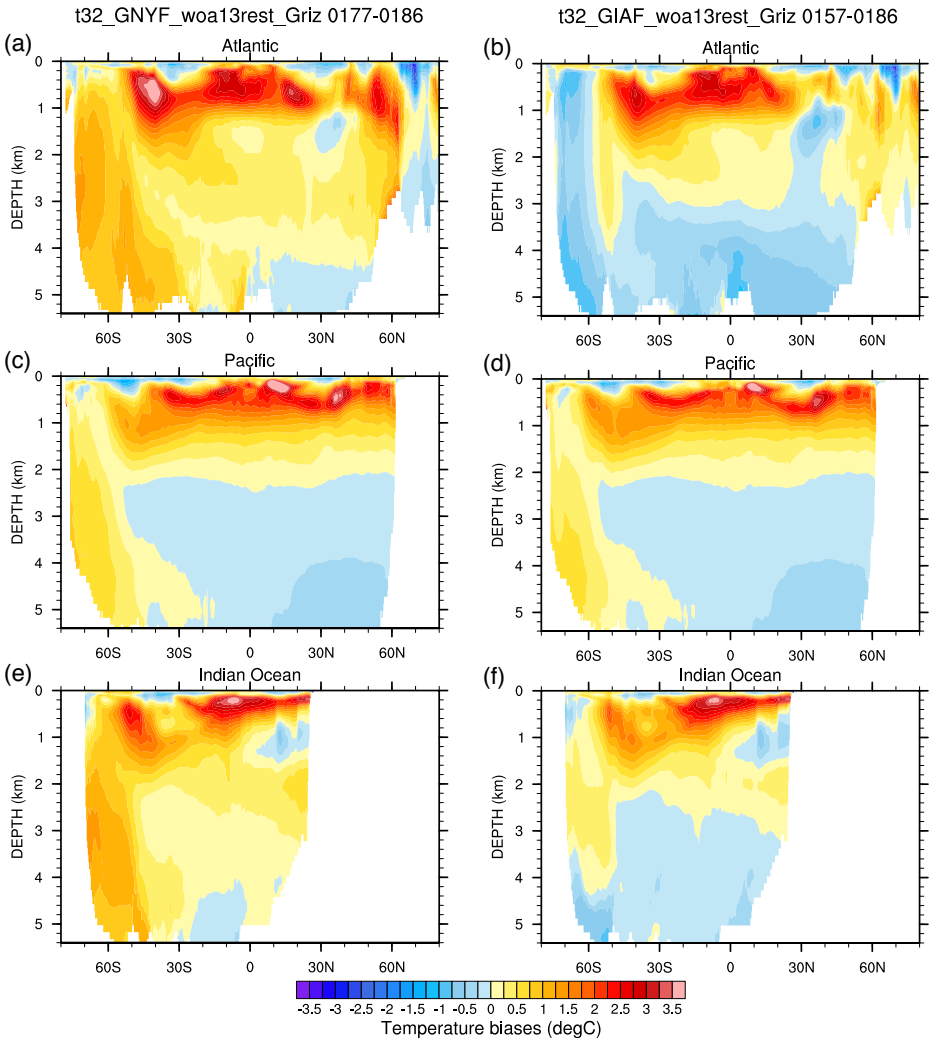

Figure 2: Climatological, zonal mean potential temperature biases against WOA13v2, for the **(a, b)** Atlantic, **(c, d)** Pacific, and **(e, f)** Indian Ocean basins in (left) the GNYF case and (right) the GIAF case. The zonal means of the Southern Ocean in each basin sector are also included.

Zonal mean temperature and salinity. The time- and zonal-mean potential temperature (θ) and salinity minus WOA13v2 climatology difference distributions in each basin are shown in Figure 2 and 3. A warm ($> +3$°C) and salty ($\sim$0.2 psu) bias in the upper 1000 m is obvious in each basin and is thicker and stronger in the Atlantic than in the other two basins. This mid-layer warm and salty bias is common in many forced ocean-sea ice (FOSI) models

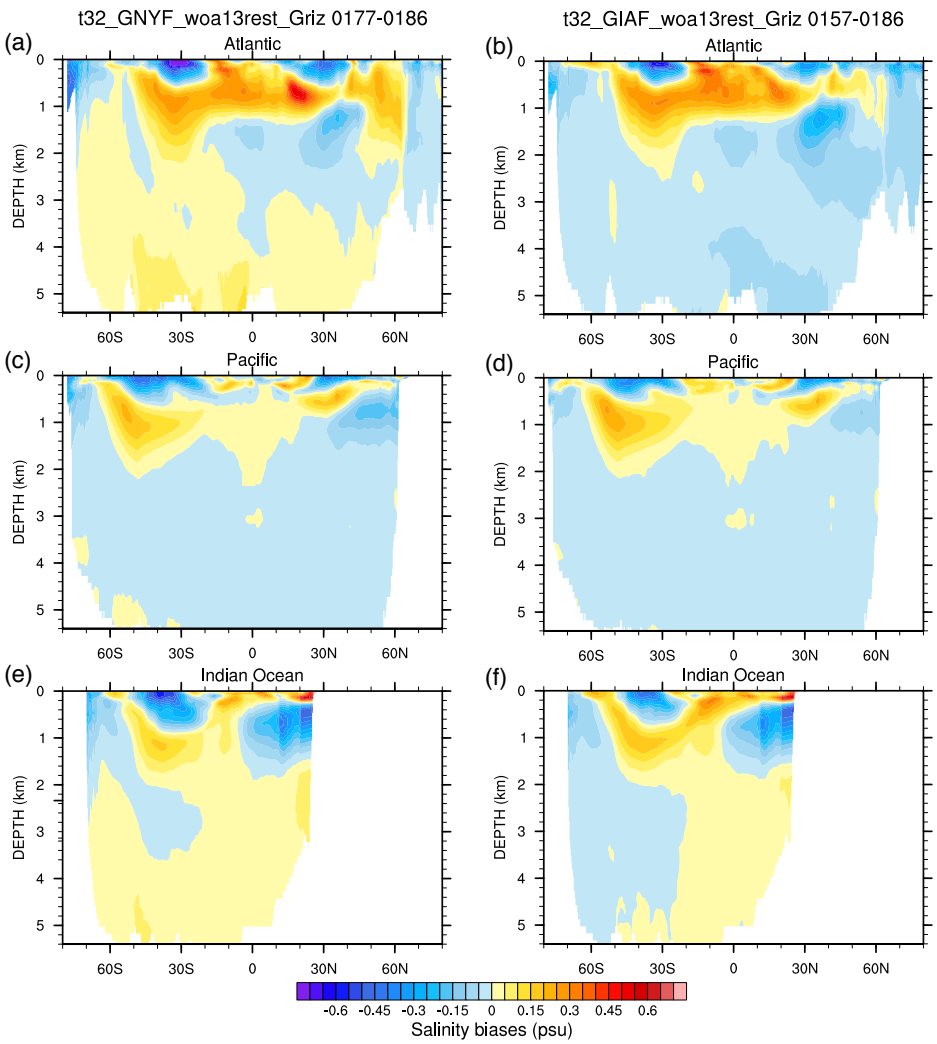

Figure 3: Same as Figure 2, but for the salinity field.

(*Danabasoglu et al.*, 2014), but we notice that the magnitude of the θ bias is stronger in HiLAT03 than in most other FOSI models. This strong θ bias is likely attributed to the fact that HiLAT03 neither fully resolves mesoscale eddies nor uses a mesoscale eddy parameterization in its tracer equation. As shown in a hierarchy of GFDL models with different ocean resolutions (*Griffies et al.*, 2015), transient mesoscale eddies act to transport heat upward and partially compensate or offset the heat transported down by the mean flow. An eddy parameterization imparts an upward heat transport and helps to reduce the mid-layer warm bias, but the effect differs systematically from that in a high resolution (e.g., 0.1°) model. But it seems that the lack of transient eddies does not result in a strong salinity bias at the same depth.

The biases below 1000 m are weak, mostly due to the fact that the simulation is still short to disturb the deep layers. The cold biases seen in most basins (Fig. 2) are due to the fact that the model is initialized from PHC2, which is overall colder below 1000 m compared

with the WOA13v2 data set. We notice that the GNYF case exhibits warm biases of ∼1°C in the Southern Ocean, especially over the Atlantic and Indian Ocean sectors (Fig. 2a and e), while such biases are not seen in the GIAF case. We suspect it is because the excessive sea ice formation immediately outside the Antarctic continent during winter (as shown in the sea ice concentration map of Fig. 13g, which will be discussed later), which helps to prevent heat loss to the atmosphere and retain heat in the intermediate and deep layers. Such excessive sea ice could also encourage deep water formation by brine rejection and cause salty biases (Fig. 3a). Previous CCSM4 simulations with 1° POP2 also reported a salty bias associated with AABW, and excessive sea ice is responsible for such a bias (*Danabasoglu et al.*, 2012). In contrast, the GIAF case has an abnormally strong deep convection over the Weddell Sea, which overwhelms this effect and results in a cold and fresh bias instead (Fig. 2b and Fig. 3b).

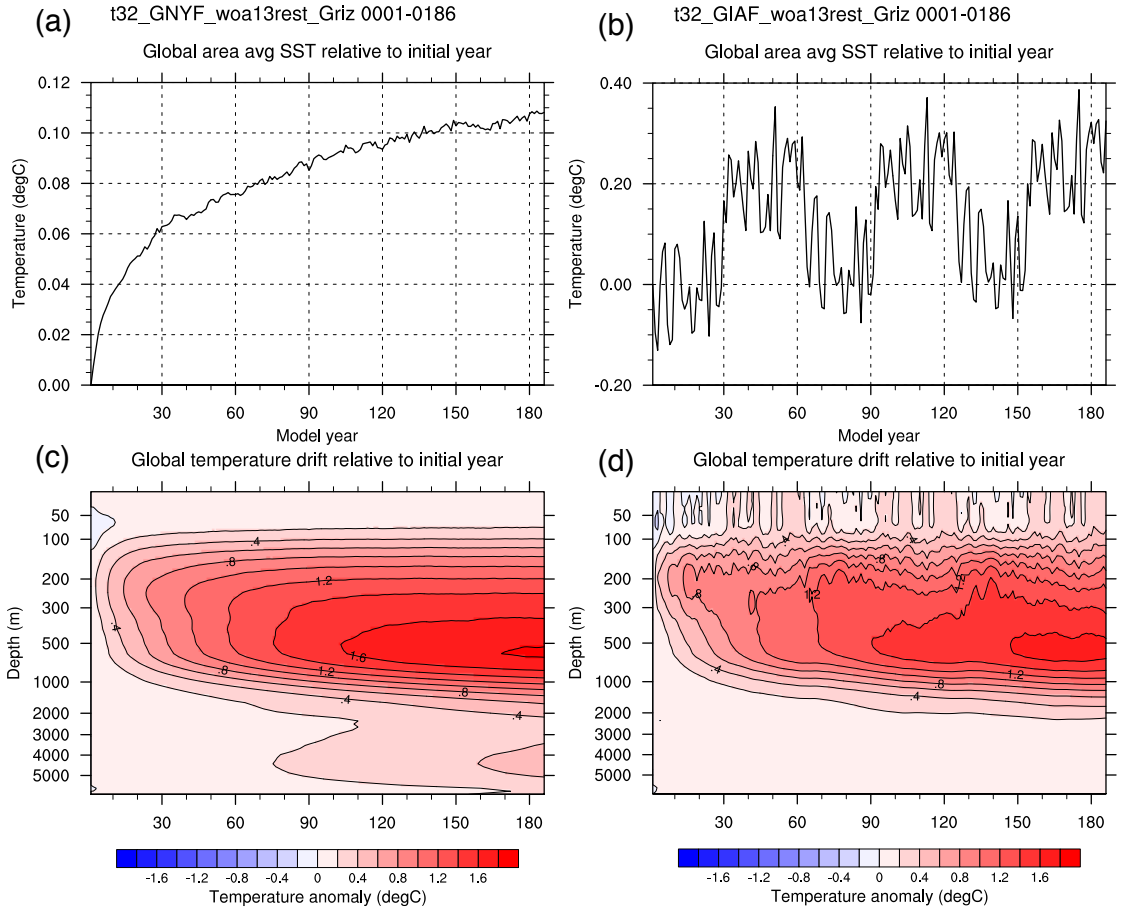

Figure 4: Global drift of the annual mean potential temperature **(a, b)** at surface and **(c, d)** as a function of depth and time, relative to the first model year for (left) GNYF and (right) GIAF. The upper 1000 m is expanded relative to the deep ocean.

Trends in globally averaged temperature and salinity. We exhibit in Figure 4 the time series from annual-mean, global-mean SST drift and the horizontal mean drift in

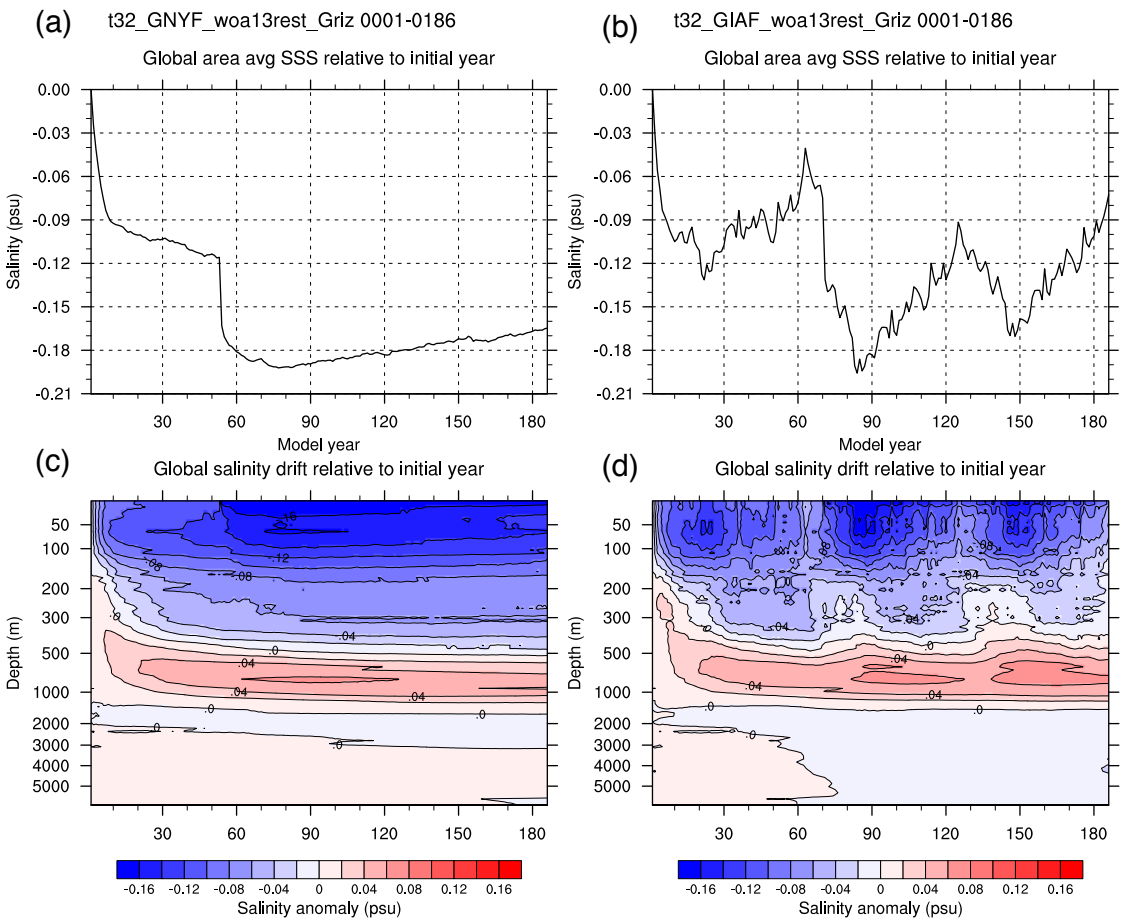

Figure 5: Same as Figure 4, but for the salinity field.

θ as a function of depth. The general warming trends at both surface and deep ocean are expected, since the ocean surface heat flux estimated by the CORE-II data set is 1 W/m^2 (*Large and Yeager*, 2009), indicating a small ocean heat uptake from the forcing itself. We further double checked the ocean volume-mean temperature, which increases from 3.603°C at the initiation to 4.12°C by the end of the 186-yr simulation, consistent with the 1 W/m^2 heat update. The SST in GNYF undergoes rapid warming in the first 30 years and slows down the warming process for the remainder of the simulation (Fig. 4a). By model year 186 the SST warming reaches slightly above 0.1°C relative to the initial state. The SST in GIAF experiences much stronger inter-annual fluctuations and exhibits periodicity corresponding to the 62-year forcing cycle (Fig. 4b). It shows rapid warming of ∼0.2°C around the 30th year of each forcing cycle, corresponding to the 1976/77 climate shift related to the Pacific Decadal Oscillation (*Newman et al.*, 2003). Between 1976 and 1977, the tropical Pacific underwent a rapid warming that had global impacts. The linear trend of SST is ∼0.1°C, consistent with the GNYF case.

Consistent with the warm θ biases at the intermediate depths discussed before (Fig. 2), the horizontal mean drift in θ as a function of depth shows that the drift maximizes at

500 m, with the value of 1.8°C in GNYF and 1.6°C in GIAF, respectively (Fig. 4c and d). Since the surface is only slightly warmed, the mid-depth warming indicates that heat is transported from the ocean surface vertically downward into the interior of the global oceans. In GNYF, a second warming centering around 4000 m becomes obvious after year 75 and reaches above 0.4°C by year 186, corresponding to the deep warming over the Southern Ocean (Fig. 2c). The temperature drift shown in CORE-II forced HiLAT03 is quite different from results from the coupled version of this model, E3SMv0-HiLAT. A 1850-control simulation of E3SMv0-HiLAT shows cooling in the upper 500 m and warming below this depth (*Hecht et al.*, 2019b). This type of upper-cooling-lower-warming drift will be discussed more in the Discussion section.

We present the salinity drift at the surface and as a function of depth in Figure 5. The SSS freshens during the initial 10 years in each of the runs. After that, SSS in GNYF undergoes a gradual freshening phase until year 54, at which point the data set that surface salinity is restored to is changed from PHC2 to WOA13v2. Such a salinity drop is expected, since SSS is fresher in WOA13v2 than in PHC2, especially over the Arctic region. After this drop, SSS displays a gradual rise for the remainder of the 186-yr simulation. In comparison, SSS in GIAF exhibits strong periodicity, similar to SST (Fig. 4b). Except for the similar salinity drop at year 71 due to the restoring change, the surface ocean in each forcing cycle exhibits a freshening trend during the first 21 years and a salinification trend during the rest of the cycle. It is unclear why such a sign switch of the multi-decadal trend occurs. The CORE forcing data does not have an apparent trend or strong interannual variations in global net freshwater flux (*Large and Yeager*, 2009), therefore such a trend swirth is likely due to salinity redistribution by the ocean circulation.

The horizontal-mean salinity drift as a function of depth shows freshening in the upper 500 m depth. A salinification of 0.06 psu between 500 – 1200 m is mostly associated with Antarctic Intermediate Water (AAIW), which is also seen in Figure 3, especially over the Atlantic basin. But the overall salinity drift is much smaller than in most coupled models, such as the coupled E3SMv0-HiLAT and the CESM1 1850 control, both of which shows drift of -0.3 psu at surface and $+0.06$ at depth (*Hecht et al.*, 2019b).

3.2 Ocean dynamics and general circulation

SSH variability. The sea surface height (SSH) variability is a direct reflection of the ocean energetic level and has been shown to be dramatically different among models ranging from 1° to 0.1° in resolution (*Smith et al.*, 2000). To accurately reproduce the SSH variability at high energetic regions such as the Agulhas leakage (warm and salty Indian Ocean waters carried to the South Atlantic), a model resolution of at least 0.1° is needed in order to resolve mesoscale dynamics, even though both 0.1° and 0.5° models produce satisfying mean SSHs (*Biastoch et al.*, 2008).

Figure 6 compares the modeled SSH variability based on 5-day averaged data of the last year of simulation (model year 186) against the satellite altimetry data AVISO (*Ducet*

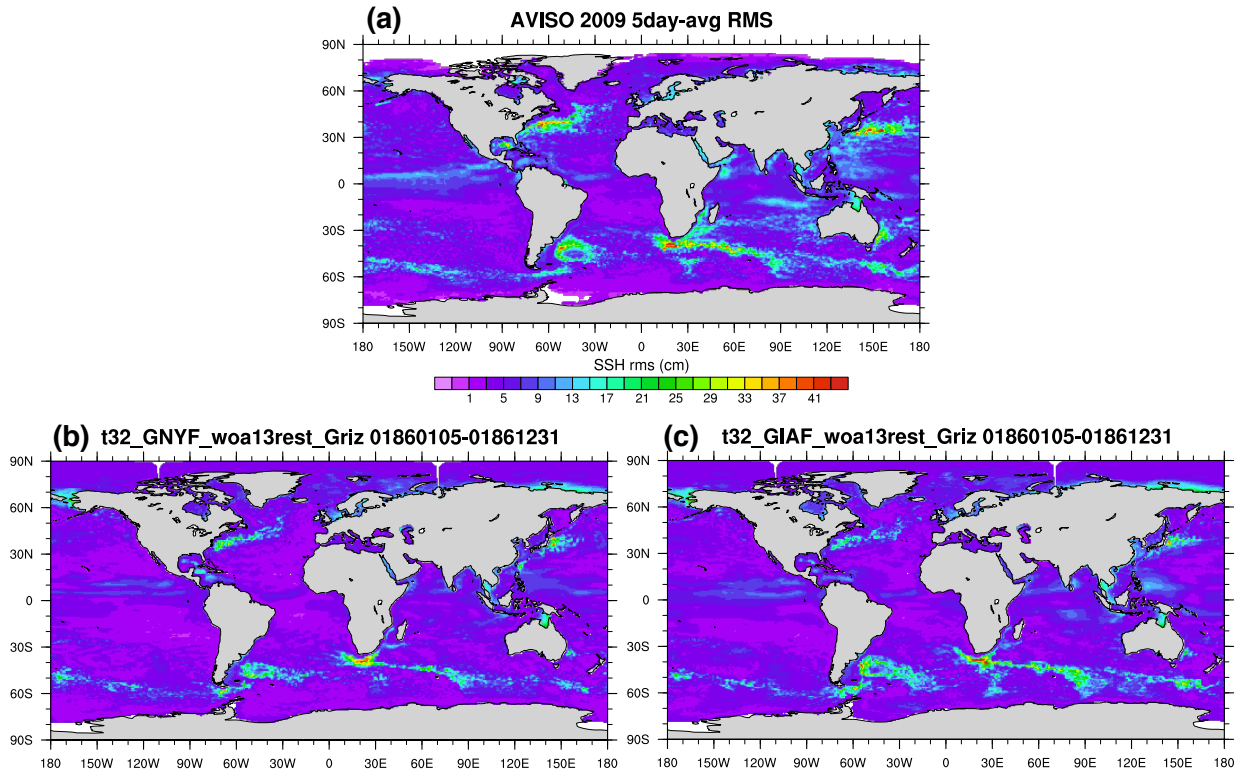

Figure 6: Sea surface height (SSH) variability based on 5-day averaged **(a)** 0.25° satellite altimetry data AVISO (*Ducet et al.*, 2000) for one year data of 2009 and **(b, c)** GNYF and GIAF output for the last year of simulation (model year 186).

et al., 2000). As expected, the model has similar geographical distributions of variability and differs primarily in amplitude, consistent with previous modeling studies (*Smith et al.*, 2000). The most noticeable differences are found at the western boundary currents (WBCs) in the Northern Hemisphere, namely the Gulf Stream and the Kuroshio. The lower amplitudes are mostly due to unresolved eddy kinetic energy, commonly found in eddy-permitting models (*Mazloff et al.*, 2010).

However, the GIAF case has a surprisingly decent representation at the Argentine Basin and the Agulhas leakage region, although the model's overall amplitude remains low in the Southern Ocean (Fig. 6c). It is likely due to the fact that these regions produce the largest mesoscale eddies in the world ocean (*Olson and Evans*, 1986) and can be well resolved by the model at this latitude. Moreover, *Pichevin et al.* (1999) indicate that Agulhas rings are generated not due to an instability associated with the breakdown of a known steady solution but rather due to the zonal momentum flux (i.e., flow force) of the Agulhas jet that curves back on itself, therefore their scale is greater than that of their classical counterparts produced by instability. The good representation implies that this model captures important dynamics at these two regions and will be useful for research topics applied here.

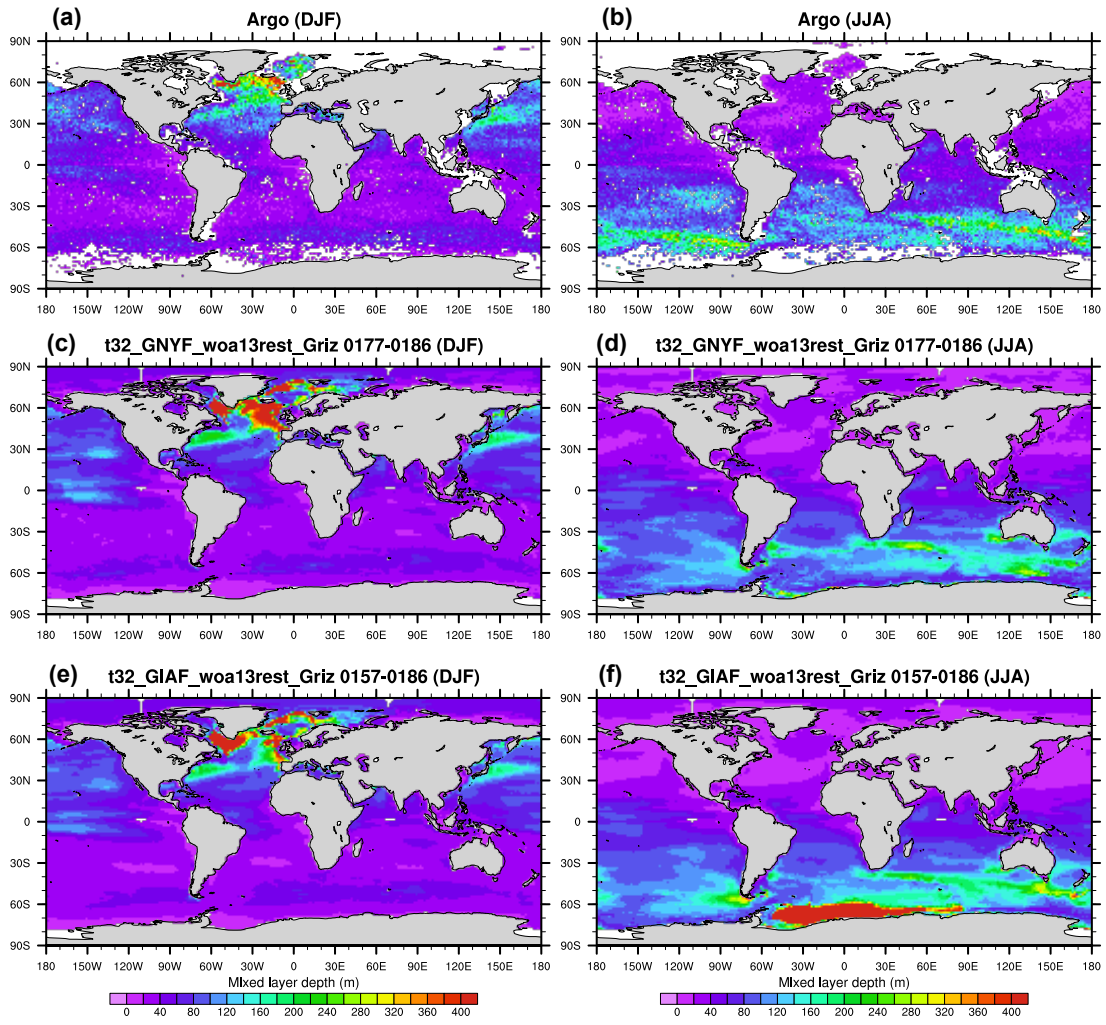

Figure 7: The climatology of the (left) boreal winter and (right) boreal summer mixed layer depth (MLD) for **(a, b)** Argo dataset through April 2018 (*Holte et al.*, 2017), **(c, d)** GNYF, and **(e, f)** GIAF.

Winter and summer MLD. The mixed layer depth (MLD) is influenced by the surface buoyancy flux and directly reflects deep water formation at high latitudes of Atlantic and the Southern Ocean. Figure 7 compares the model climatology of the boreal winter (DJF) and summer (JJA) MLD against the Argo dataset through April 2018 (*Holte et al.*, 2017). The model MLD agrees well in the overall distribution patterns with observation. The model produces deeper MLDs at the deep water formation regions in the North Atlantic during winter time, which is a bias commonly found in FOSI simulations (*Danabasoglu et al.*, 2014) possibly due to the lack of feedback to the atmospheric forcing. However, the deep winter MLDs over the deep water formation regions, especially the nearly-top-to-bottom MLD over the Labrador Sea in March (not shown here), do not result in an overly vigorous AMOC (Fig. 10), because the deep MLDs do not necessarily represent actual water transformation, and even if water transformation occurs in the model, it does not necessarily indicate a contribution to the AMOC intensity. This is consistent with recent observational (*Zantopp*

et al., 2017; *Lozier et al.*, 2019) and modelling findings (*Pickart and Spall*, 2007; *Zou and Lozier*, 2016).

In the Southern Hemisphere, the magnitude of the summer-time MLDs along the ACC path, which used to be notably shallow in 1° meshes of previous CCSM versions (*Danabasoglu et al.*, 2012), are improved in this model and are comparable to the observation (Fig. 7 d and f). Abnormally deep, geographically large MLDs over the Weddell Sea occurs in the GIAF case. This deep convection phenomenon, found in this particular case, will be discussed in Section (cite section number).

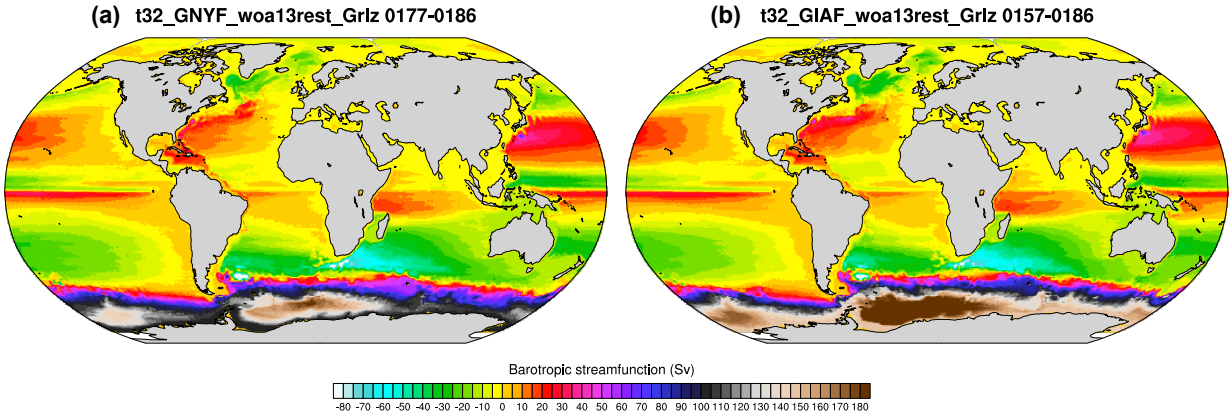

Figure 8: Mean barotropic (vertically-integrated) streamfunction (BSF; in Sv) in **(a)** GNYF and **(b)** GIAF.

Horizontal general circulation. The large-scale horizontal ocean circulation is assessed in terms of barotropic streamfunction (BSF; Fig. 8). In general, the BSF in HiLAT03 model simulations is similar to those produced by other coupled and forced ocean models (e.g., *Griffies et al.*, 2009; *Sidorenko et al.*, 2015), with some differences in the strength of the main gyres (Table 2). HiLAT03 simulates the North Atlantic subtropical gyre with a maximum of 47 and 57 Sv for the GNYF and GIAF cases, respectively. To compare with other FOSI models, we further search the values of maximum transport of subtropical gyre between 80°–60°W at 34°N as defined in *Danabasoglu et al.* (2014). These values are 34 Sv (GNYF) and 36 Sv (GIAF) in HiLAT03, falling in the multi-model range from 17 to 40 Sv (*Danabasoglu et al.*, 2014). The North Atlantic subpolar gyres in both GNYF and GIAF cases are similar, with maximum values of 33 and 34 Sv, respectively. Once following the convention of the multi-model comparison, which is 65°–40°W at 53°N, HiLAT03 produces 29 (GNYF) and 31 (GIAF) Sv, also falling in the multi-model range of 12 to 44 Sv (*Danabasoglu et al.*, 2014). One point worth mentioning is that the strength of the subtropical gyre is comparable to that of the 1° POP2 (35 Sv), but the strength of the subpolar gyre is much weaker than that in 1° POP2 (41 Sv).

The subtropical gyres in the North Pacific maximizes along Kuroshio to the south of Japan, with values of 74.8 Sv (GNYF) and 68.8 Sv (GIAF). Both cases exhibit obvious

Table 2: Strength (in Sv) of the North Atlantic subtropical gyre (STG) and subpolar gyre (SPG) as estimated by the barotropic streamfunction, in two cases of HiLAT03 and other CORE-II forced models (*Danabasoglu et al.*, 2014). Following the convention of *Danabasoglu et al.* (2014), the strength of the STG is searched between 80°–60°W at 34°N, and that of the SPG is searched between 65°–40°W at 53°N.

	HiLAT03		1° POP2	Multi-model range
	GNYF	GIAF		
STG	34	36	35	17–40
SPG	29	31	41	12–44

meanders along the Kuroshio Extension region. Maximum BSF values are found in the Southern Ocean regions, consistent with other models. It is noticed that the GIAF exhibits an abnormaly strong gyre over the Weddell Sea, which is closely related to the super strong convection over there, and will be discussed later.

Meridional overturning circulations. The time-mean global MOC and the AMOC distributions in HiLAT03 are shown in Figure 9. The global MOC structure (Fig. 9a and b) is similar to previous fully-coupled (CCSM3, CCSM4) and forced 1° POP2 results (*Danabasoglu et al.*, 2012). The strength of the overturning cell at the latitudes of the ACC in both GNYF ($>$ 24 Sv) and GIAF ($>$ 28 Sv) is larger than that of the forced 1° POP2 ($>$ 20 Sv). This is likely due to the fact that the cell represents a residual circulation, that is, the sum of the wind-driven overturning (Deacon Cell) and the parameterized eddy contributions, in the 1° POP2. In contrast, HiLAT03 cannot fully resolve mesoscale eddies at these latitudes and has mostly the Deacon Cell.

The AMOC structure in HiLAT03 (Fig. 9c and d) is also similar to previous POP2 results (*Danabasoglu et al.*, 2012, 2014), in terms of the location of the maximum transport associated with the North Atlantic Deep Water (NADW), as well as the NADW penetration depth. The maximum NADW transport magnitudes are 20 and 16 Sv in GNYF and GIAF, respectively, both weaker than the 1° POP2 (28 Sv) (*Danabasoglu et al.*, 2012, 2014). This magnitude reduction with increased model resolution also occurs in GFDL models (from CM2.1 with 1° ocean to CM2.5 with 0.25° ocean) (*Delworth et al.*, 2012), and the insufficiently resolved overflows of dense water from the Nordic Seas may be the reason. In low resolution models, overflow parameterization helps to move dense water to the North Atlantic, while this parameterization is turned off in HiLAT03. The reason why the magnitude in GIAF is weaker than that in GNYF is unclear. GIAF exhibits a relatively strong counterclockwise cell associated with Antarctic Bottom Water (AABW) (Fig. 9b and d), which is due to the overly strong deep convection over the Weddell Sea. But over the model running time scale of 186 years, it is unlikely that this overly strong AABW in GIAF could affect the NADW formation by much.

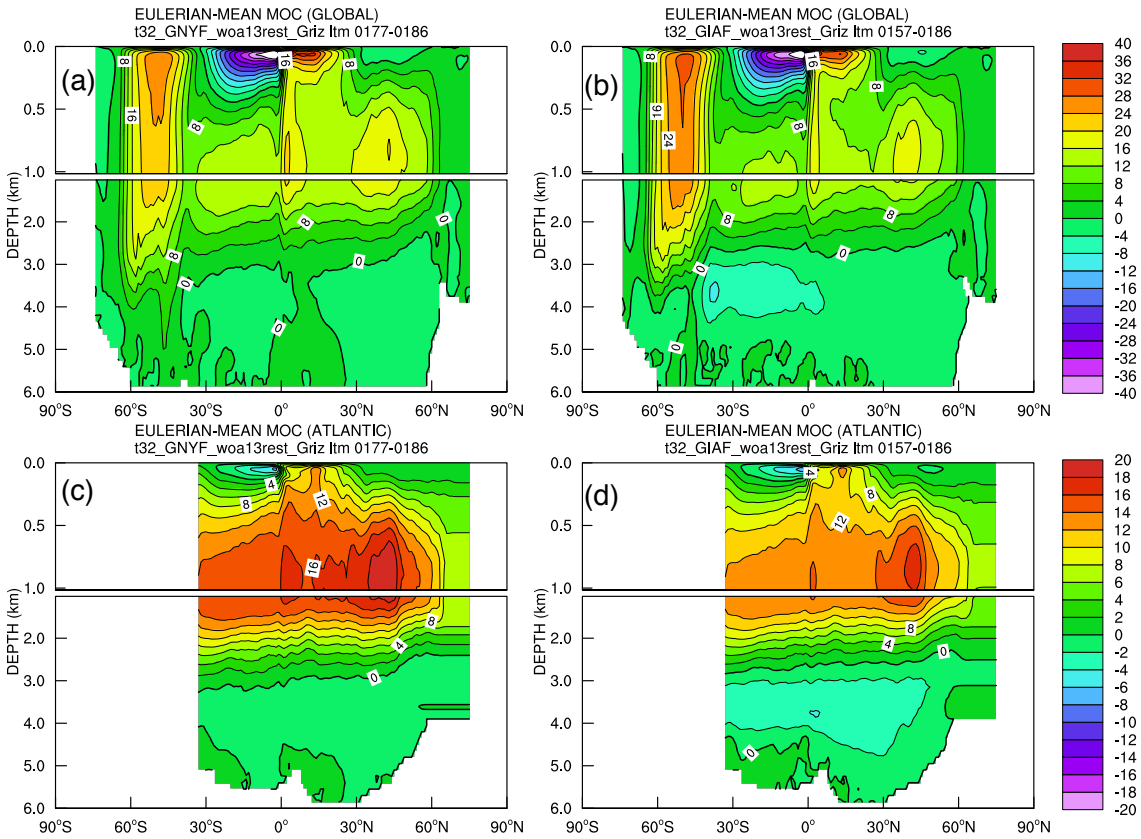

Figure 9: Climatological zonally-integrated meridional overturning circulation for the **(a, b)** global and **(c, d)** Atlantic Oceans from (left) GNYF and (right) GIAF. Since neither mesoscale nor submesoscale parameterization is employed, the Eulerian-mean component is the total.

The time series of the AMOC intensity, which is searched as the maximum transport below 500 m in the North Atlantic, in different cases are shown in Figure 10a. The AMOC intensity at 26°N is also computed (Fig. 10b) in order to be quantitatively compared with the Rapid Climate Change (RAPID) mooring array data at this latitude (*Smeed et al.*, 2017). As expected, the AMOC in GNYF lacks inter-annual variability and constantly increases with time. By the end of the simulation, the maximum AMOC reaches ∼19.5 Sv and the AMOC at 26°N reaches 16 Sv, comparable to the RAPID mean. In contrast, the AMOC in GIAF exhibits strong inter-annual variability, and there is no obvious trend across the simulation. The inter-annual variability at 26°N (ref curve in Fig. 10b) is milder compared with that of the maximum AMOC (ref curve in Fig. 10a), and the variations over the last 6 years (corresponding to 2004–2009) seem consistent with the RAPID data except that the absolute values are systematically smaller by ∼3 Sv. The time series of the lower cell intensity, which is searched as the minimum transport below 3000 m in the South Atlantic and represents the AABW transport, are shown in Fig. 10c. The GNYF case shows fairly stable lower cell across the simulation with the value of 2 Sv. However, due to the super strong deep convection and the AABW formation in GIAF starting the middle of the forcing

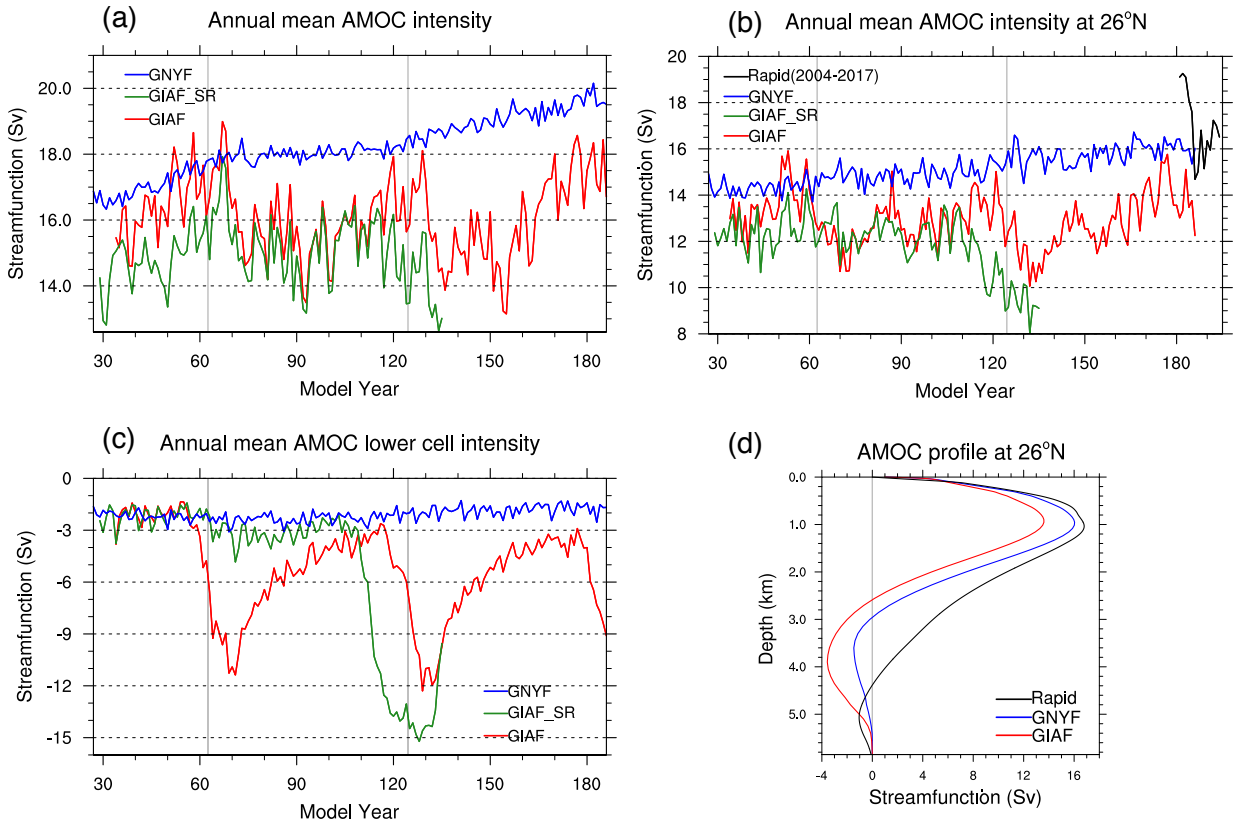

Figure 10: Annual mean Atlantic Meridional Overturning Circulation (AMOC) intensity of **(a)** the upper cell maximum, **(b)** the upper cell at 26°N, and **(c)** the lower cell minimum. Gray vertical lines indicate the CORE-II inter-annual forcing cycles. Negative values in **(c)** indicates counterclockwise circulation. **(d)** Climatological AMOC profiles at 26°N. In **(b)** and **(d)**, model results are compared with the RAPID data of April 2004–February 2017 (*Smeed et al.*, 2017). In **(d)**, we use the model climatology in GNYF (last 10 years) and GIAF (last 30 years).

cycle, the lower cell gets abnormally strong (up to 10–12 Sv) towards the end of the forcing cycle, and persists for a few decades after the next cycle starts. Details will be further discussed shortly.

Fig. 10d provides a comparison of the AMOC climatological profiles in HiALT03 with the profile based on the RAPID data (*Smeed et al.*, 2017). The RAPID estimate for the NADW maximum transport averaged between April 2004 and February 2017 is 16.8 Sv, occurring at 1030 m depth. The general shape and the depth of the maximum value of the RAPID profile are well captured by HiLAT03, but with underestimated values of 16.0 Sv (GNYF) and 13.6 Sv (GIAF). This underestimation has been reported in many FOSI models (*Danabasoglu et al.*, 2014), but not in the 1° POP2, which produces the maximum transport as high as 18.6 Sv. Again, this is possibly because the HiLAT03 profile is for the Eulerian-mean component only while the 1° POP2 accounts for both the Eulerian-mean and the eddy components, although the eddy contributions are very small at this latitude. It is quite evident that the NADW penetration depth in HiLAT03 is ∼1500 m shallower than in

RAPID, which is also found in many FOSI models, and the insufficiently resolved overflows of dense water from the Nordic Seas may be the reason. Instead, the 1° POP2 employs an overflow parameterization to represent the Nordic Seas overflows (*Yeager and Danabasoglu*, 2012) and produces a more reasonable penetration. Associated with the shallow NADW, the AABW occupies the deep ocean below 3000 m, which in RAPID profile AABW is confined below 4400 m. The overly strong AABW maximum transport in GIAF associated with the abnormally strong deep convection in the Weddell Sea is obvious.

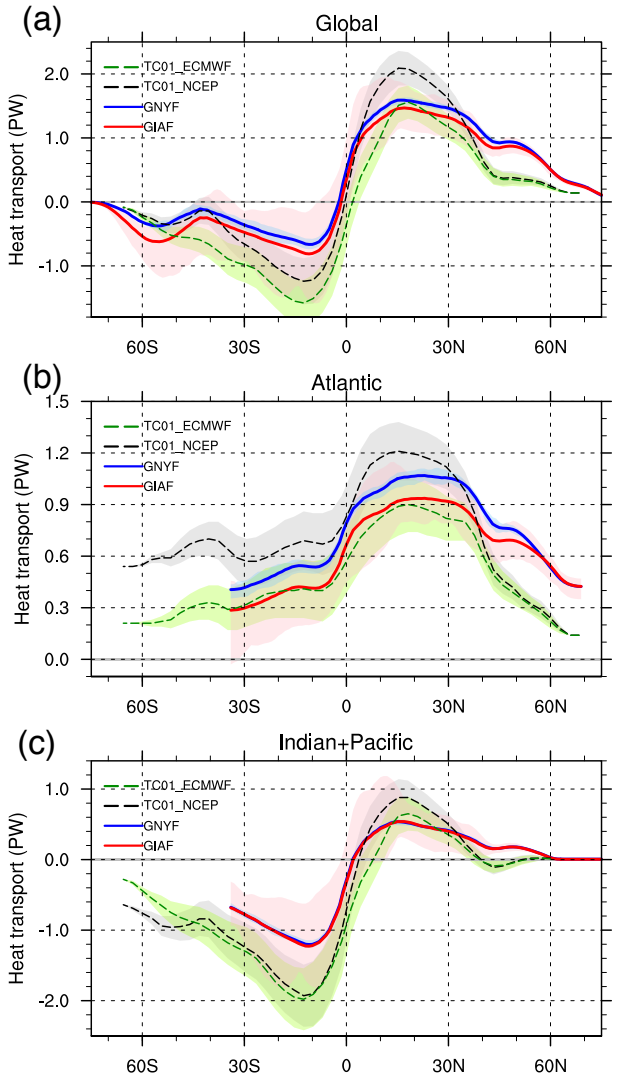

Figure 11: Climatological meridional heat transports (MHT, positive northward) in PW (10^{15} W) for the **(a)** global, **(b)** Atlantic, and **(c)** Indo-Pacific Oceans. The (blue) GNYF and (red) GIAF results are compared with the estimates from both (black) NCEP and (green) ECMWF atmospheric reanalysis using the period of February 1985 to April 1989 (TC01; *Trenberth and Caron*, 2001). Shading of the model results indicates the maximum-minimum range found in the annual mean, and shading of TC01 estimates indicates 1σ error envelope.

Meridional heat transport. Previous model studies have shown an explicit dependence of ocean meridional heat transport (MHT) on resolution, ranging between 4° and 0.1° (*Fanning and Weaver*, 1997; *Bryan and Smith*, 1998). But *Gent et al.* (1999) has pointed out that this dependence appears to be much weaker when more advanced sub-grid scale mixing parameterizations (such as the GM parameterization) are used. One major difference of HiLAT03 from the 1° POP2 and most other eddy-permitting models is that it does not include

such a sub-grid scale mixing parameterization to represent the horizontal tracer diffusion. Therefore, with that setup, whether HiLAT03 is still able to produce reasonable MHT is one of the most important merits to assess.

Figure 11 presents the global zonally-averaged MHT, as well as in Atlantic and Indo-Pacific, and compares with the estimates from both NCEP and ECMWF atmospheric reanalysis using the period of February 1985 to April 1989 (*Trenberth and Caron*, 2001). The global MHT of HiLAT03 overall falls in the estimate range except from 40°N northward, and this high latitude mismatch lies in the Atlantic (Fig. 11b). The model MHT peaks at 25°N with the values of 1.59 PW (GNYF) and 1.47 PW (GIAF), consistent with the ECMWF-based estimates while smaller than the NCEP-based estimates. In comparison, the 1° POP2 has the peak transport of 1.62 PW (*Danabasoglu et al.*, 2012), while the CM2.5 (GFDL coupled model with 0.25° ocean) produces the peak transport of 1.7 PW (*Griffies et al.*, 2015), both higher than HiLAT03 does.

In the Southern Hemisphere, the peak transports are slightly displaced northward at 10°S, with values (−0.66 PW in GNYF and −0.81 PW in GIAF) falling above the estimated range. These low latitude mismatch is mostly due to the weak MHT in the Indo-Pacific Oceans (Fig. 11c). We note that the reanalysis-based estimates can be quite different in the Southern Hemisphere depending on the reanalysis data set. For example, the implied southward transport estimates from *Large and Yeager* (2009) calculated using the CORE inter-annual fluxes for the 1984–2006 period have a peak value of only 0.35 PW, much lower than the estimates used here.

In the Atlantic, HiLAT03 shows reasonable MHT in comparison with the estimated range (Fig. 11b). If compared with the observation-based estimates (not shown here), HiLAT03 is close to the lower end of the range. Considering the overall weak AMOC and no mesoscale eddy parameterization in HiLAT03, the reasonable MHT is surprising to some extent. Our explanation is that the the reasonable MHT is largely due to the gyre transport associated with the subsurface warm bias, which compensates the effects of overturning and eddy parameterization. HiLAT03 exhibits a broad span of peak transports from 15 to 35°N, different from all other FOSI models (*Danabasoglu et al.*, 2014) and coupled models (*Danabasoglu et al.*, 2012; *Griffies et al.*, 2015) as well as the analysis-based estimates that all show a single peak transport around 20°N. The higher-than-estimate values at 40°N northward in HiLAT03 are also found in many advanced models like CESM/CCSM and GFDL models (*Danabasoglu et al.*, 2012; *Griffies et al.*, 2015), and are in agreement with *Ganachaud and Wunsch* (2003) at 45°N. In this case, the observation-based estimate at 45°N is 0.6 PW (*Ganachaud and Wunsch*, 2003), much higher than the analysis-based estimates. As noted in *Griffies et al.* (2009), there are a lot of limitations to using the analysis-based estimates, and observation-based estimates are more reliable where analysis-based estimates are not consistent. The MHT in GNYF is overall higher at each latitude than in GIAF, mostly due to the fact that the AMOC is stronger in GNYF.

3.3 Antarctic prolonged polynyas in GIAF

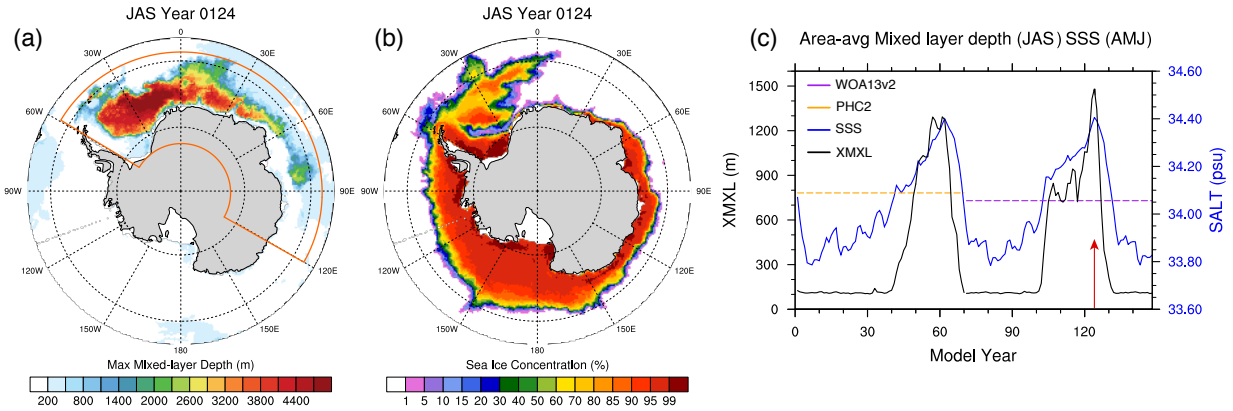

Figure 12: The Antarctic prolonged polynyas in the GIAF case, shown by the July–September **(a)** maximum mixed-layer depth (XMXL) and **(b)** sea ice concentration of the model year 124 as an example, which has a strong polynya event (time indicated by the red arrow in **c**) and corresponds to the last year of the second CORE forcing cycle. The orange box in **a** indicates the region where the averaged variables of **c** are calculated. **(c)** Time series of the July–September XMXL (black) and April–June SSS (blue) averaged over the Weddell Sea and the Indian sector of the Southern Ocean, as indicated by the orange box in **a**. The first two cycles of the model output are shown. The area-averaged SSS of the PHC2 and WOA13v2 data sets, which are used for surface salinity restoring in the GIAF case, are also shown here for comparison.

As mentioned in previous sections, the GIAF case simulates an abnormally strong, wide, and prolonged deep convection area over the Weddell Sea and the Indian Ocean sector of the Southern Ocean, during austral winter of the latter half of each CORE forcing cycle. It resembles many features of the Weddell Sea polynya, which refers to the large sea-ice free area that occurred in the open-ocean region of the Weddell Sea in the winters of 1974–76 (*Carsey*, 1980), except that it is much longer and wider; we refer to it as the "Antarctic prolonged polynya". Strong and prolonged Weddell polynyas have also been simulated in other coupled Earth System Model simulations, although they usually disappear after a ∼10 year cycle. In this section, we describe the spatial and temporal characteristics of the Antarctic prolonged polynya, its local and remote impacts, and finally discuss possible causes.

Open-ocean polynyas are initiated through oceanic deep convection and therefore characterized by a deep ocean mixed layer; for example, the ocean mixed layer extended to 3000 m depth during the 1974–76 Weddell Sea Polynya. In this model, we use the July–September (JAS) maximum mixed-layer depth (XMXL) averaged over the region between the Antarctic coast and 58°S, and between 60°W and 120°E (the orange box in Fig. 12a), as an index for the polynya events (Fig. 12c). The polynya starts from the 40th year of the simulation (calendar year 1987), grows to its maximum by year 55 (calendar year 2002), and ends at year 63 when the second cycle of the forcing starts. During the second and the third cycles (third cycle not shown), similar polynyas occur at the same timing (from calendar year 1987 to the end of the cycle). The repeated behavior of the polynya initiation indicates that specific atmospheric conditions are favorable for polynyas to appear, but specific oceanic conditions

must also exist to allow for the polynya to sustain itself for such a long time. We select the model year 124 which has the strongest polynya (red arrow in Fig. 12c) and plot the XMXL field to show its spatial distribution (Fig. 12a). The deepest convection occurs at the east side of the Weddell Sea and extends to 4700 m depth, and horizontally covers the middle to east Weddell Sea and expands to 90°E.

Such intense and prolonged polynyas have strong local and remote effects. The deep oceanic convection allows for relatively warm (with respect to the surface) deep waters to upwell to the upper ocean, leading to surface warming (Fig. 1b) and preventing sea ice from forming during austral winter (Fig. 12b). This is the main cause of the sea ice biases found in the Southern Hemisphere of the GIAF case regarding the low ice concentration (Fig. 13k) and low ice thickness (Fig. 15k), and therefore low ice volume as a result (Fig. 16e). The prolonged polynya actively mixes the water column and upwells the heat in the deep Southern Ocean, therefore partially (Indian Ocean sector) or even completely (Atlantic sector) compensates the warm biases that have been found in the GNYF case (Fig. 2). The well-mixed water column also weakens the stratification and promotes barotropic flows, as seen by a strong Antarctic Circumpolar Current as well as an intense Weddell Gyre (over 180 Sv) (Fig. 8). A large volume of dense bottom water is produced in the polynya and transported northward (*Hirabara et al.*, 2012), resulting in a strong bottom overturning circulation in the Atlantic with a maximum intensity of 11 Sv (Fig. 10c).

Previous modeling studies suggest that salinity above the shallow pycnocline is an important factor for preconditioning the Weddell Polynya formation after ice-covered winters (*Kurtakoti et al.*, 2018; *Hirabara et al.*, 2012). Figure 12c shows the time series of the austral fall season (April–June) SSS over the same region as where XMXL is calculated. The fall-season SSS drops below the observational data within a few years after the cycle is initialized. The surface salinity restoring acts to inject net salt flux into the upper ocean, possibly preconditioning the surface layer.

In order to test the model's sensitivity to surface salinity restoring, we performed a test of GIAF_SR, where SSS is not just restored in ice-free regions, but also under sea ice with the same intensity as in the open ocean. That is, the model has a global restoring with an intensity of 4 years. We used Year 29 of GIAF as the initial conditions, and performed the simulation for 107 years. In this test, the prolonged polynya does not occur during the first cycle. However, it occurs during the second cycle, with an earlier timing and an even stronger intensity, as shown in the time series of the AMOC lower cell intensity (Fig. 10c). The strong AABW formation and its northward penetration brings the AMOC lower cell up to 15 Sv, and significantly reduces the upper cell intensity to only 8 Sv (Fig. 10b). It is so far unclear which setting of restoring intensity, including its time scale and its applied region, could prevent such a prolonged polynya to occur.

There are other factors that could be important for triggering and sustaining the prolonged polynyas. Wind stress curl is a typical mechanism considered for these polynyas (*Cheon et al.*, 2015). A strong negative wind stress curl over the Weddell Sea could intensify the gyre and cause upwelling of the warm and salty deep water. Another mechanism is the

heat content accumulated in the intermediate to deep depths, which provides a heat reservoir and preconditions its occurrence (e.g., *Kurtakoti et al.*, 2018). Further investigation beyond the purposes of this report is necessary to pinpoint the Antarctic prolonged polynya initiation process and also the mechanism sustaining its presence for such a prolonged period of time.

4 Model Sea Ice Climatology

Since the launch of satellite observations of sea ice concentration in 1974, the sea ice concentration in the Arctic has experienced significant decline (*Parkinson et al.*, 1999; *Comiso and Nishio*, 2008). September sea ice extent record minimums have been established over and over again since 2005. In 2007 sea ice extent about 20% below the 2005 minimum was observed (*Comiso et al.*, 2008; *Stroeve et al.*, 2008), and then in 2012 the extent was about 30% below the 2005 minimum. By contrast, the trends around the Antarctica are not uniform, with a decreasing trend in the Amundsen-Bellingshausen Sea and an increasing trend in the Ross Sea (*Abram et al.*, 2013; *Comiso and Nishio*, 2008). In this sense, evaluating naturally fast-changing variables in models are difficult. Moreover, the accelerated Arctic sea ice retreat and the uneven Antarctic sea ice change involve linked dynamical and thermodynamical processes and feedbacks (*Steele et al.*, 2010; *Smedsrud et al.*, 2011; *Carmack et al.*, 2015), which are difficult to simulate in models. In this section, we focus on the sea ice concentration and thickness, as well as the seasonal cycles of extent and volume evaluated based on concentration and thickness. We will compare the two simulations in HiLAT03 with the CCSM4 late-twentieth-century simulation that uses 1° POP2 and CICE4 (*Jahn et al.*, 2012), and FOSI simulations with other models (*Wang et al.*, 2016a; *Downes et al.*, 2015).

4.1 Sea ice concentration and extent

Winter and summer sea ice concentrations. To assess the sea ice concentration in HiLAT03, we use satellite estimates from Nimbus-7 Scanning Multichannel Microwave Radiometer (SMMR) and Defense Meteorological Satellite Program (DMSP) SSM/I-SSMIS passive microwave data, version 1 (*Cavalieri et al.*, 1999) during the period 1978–2014 (Fig. 13a to d). The climatology in HiLAT03 uses the same definition as previous sections, namely the last 10 years (Fig. 13e to h) in GNYF and the last 30 years in GIAF (corresponding to 1980–2009, slightly shorter than the observational coverage) (Fig. 13i to l).

In general, we find that the spatial patterns as well as the 15% ice concentration edges in both hemispheres during winter time are in close agreement with the observation, while the summer patterns are less consistent, especially in the Southern Hemisphere. Winter Arctic patterns in GNYF and GIAF are quite similar, with slightly higher concentrations in central

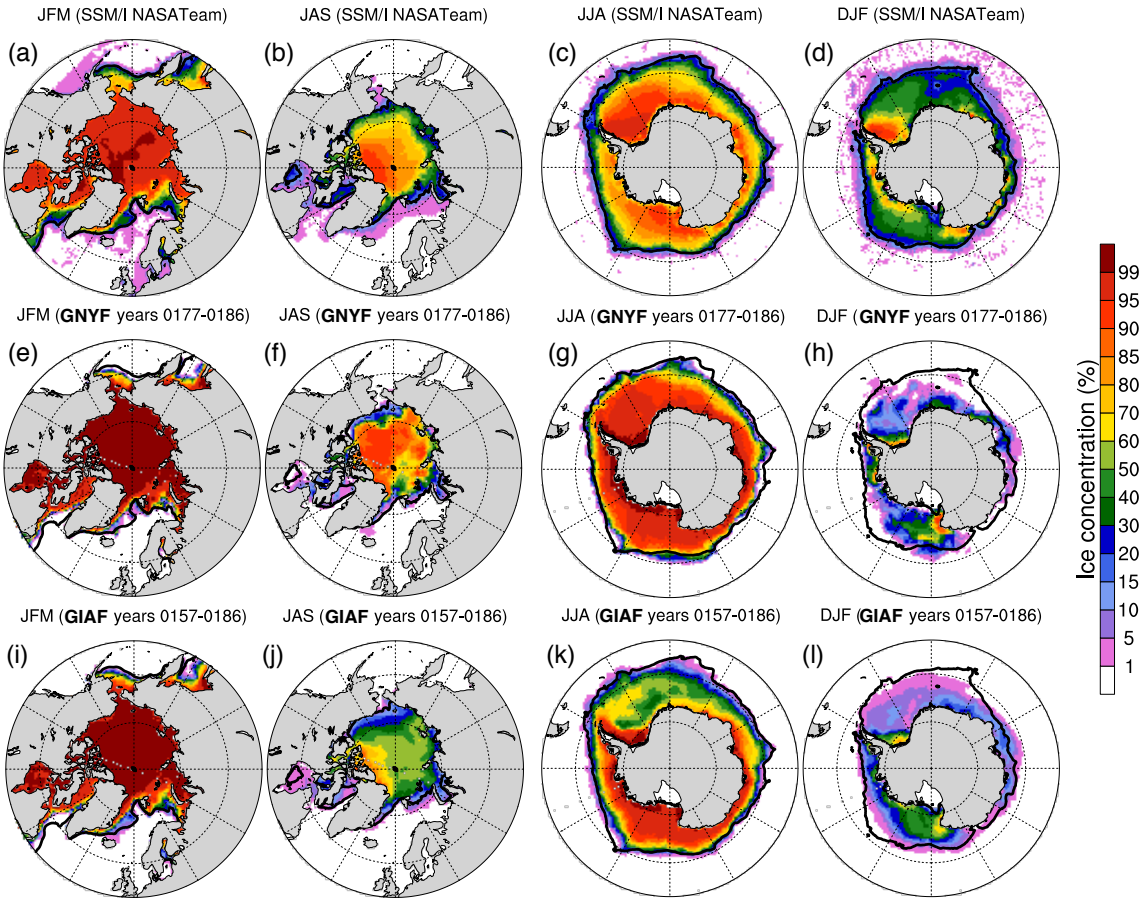

Figure 13: Climatological winter and summer sea ice concentration (%) of **(a–d)** SSM/I and SSMR (*Cavalieri et al.*, 1999) satellite estimates averaged over the 1978–2014 period, **(e–h)** GNYF, and **(i–l)** GIAF in the (left) Northern and (right) Southern Hemispheres. The black contour shows the ice edge, taken as 15% contour from the SSM/I and SSMR dataset. In the Northern Hemisphere, winter and summer are defined as January–March and July–September, respectively. In the Southern Hemisphere, these definitions change to June–August and December–February instead. Note that the color scale is nonlinear.

Arctic and less or even missing sea ice in the Labrador Sea compared with observations (Fig. 13, first column). The gradient near the sea ice edges are sharper in the model than in observation, suggesting that the model migrates from a fully-coverage region to an ice-free region within a short distance. But it worth mentioning that satellites have difficulty distinguishing ice concentration when the ice is thin and this would artificially blur the boundary to some extent. The summer Arctic pattern in GIAF is more consistent with observation than in GNYF, despite the systematically smaller values (Fig. 13, second column).

It is worth pointing out that FOSI models which use CICE4 as their sea ice components (e.g., Bergen, CMCC, and NCAR) tend to show much less sea ice concentrations during summer time than both the observation and many other models (*Wang et al.*, 2016a). In Table 3 we list the mean, standard deviation, and linear trend of the period 1979–2003 in the observation, NCAR model that uses CICE4, and the current HiLAT03 model that uses

Table 3: The mean (in 10^6 km^2), standard deviation (STD), and linear trend (in 10^4 km^2/year) of the Northern Hemisphere sea ice extent, in the GIAF case of HiLAT03 and the 1° CICE4, compared against observations (*Wang et al.*, 2016a). The statistics are calculated for September and March monthly data separately. All calculations use the period 1979–2003.

		Observation	NCAR 1° (CICE4)	HiLAT03 (CICE5)
September	Mean	6.95	3.99	5.46
	STD	0.58	1.44	1.21
	Trend	−5.3	−11.0	−10.42
March	Mean	15.72	15.20	14.90
	STD	0.34	0.22	0.29
	Trend	−3.4	−1.4	−2.04

CICE5. Most indices have been improved in the current model except for the mean value in March, and the improvement are significant in the September mean and March trend. Such improvements could be due to 1) improved physical processes from CICE4 to CICE5, 2) optimized parameter combinations, 3) refined model resolution, or 4) some combination of these factors. Detailed model comparisons are needed in the future to evaluate these factors.

In the Southern Hemisphere, the winter-time concentrations close to the continent are higher than in observation (Fig. 13, third column). GIAF simulates reduced sea ice concentration in the Weddell Sea related to the prolonged polynyas. The summer concentrations, instead, are less realistic, with generally lower values than the observations (Fig. 13, rightmost column). Such a summer-time bias has been found in most of other FOSI models (*Downes et al.*, 2015), and is largely due to the small scale processes during summer which are not realistically represented in the CORE-II forcing (*Stössel et al.*, 2011). As discussed in *Downes et al.* (2015), improvement of the summer sea ice representation requires both high resolution ocean models and a higher resolution wind forcing that incorporates the effects of katabatic winds at the Antarctic continental margin.

Ice extent seasonal cycle To quantitatively evaluate the temporal variability, we further calculate the seasonal cycle and the September time series of sea ice extent, defined as the model grid area which has at least 15% ice concentration (Fig. 14). We compare the model results with the sea ice index, version 3 (*Fetterer et al.*, 2017) for the 1979–2009 period, which is calculated based on sea ice concentrations from Nimbus-7 SMMR and DMSP SSM/I-SSMIS passive microwave data. It is worth mentioning that 'ice extent' is different from 'ice area', where the latter accounts for only the sea ice area instead of the entire ocean grid area, although both of them have a 15% criterion of ice concentration. Therefore, the total ice extent is usually greater than the total ice area.

In the Northern Hemisphere, the HiLAT03 model shows maximum and minimum ice extent in March and September, respectively, consistent with the observation, except that

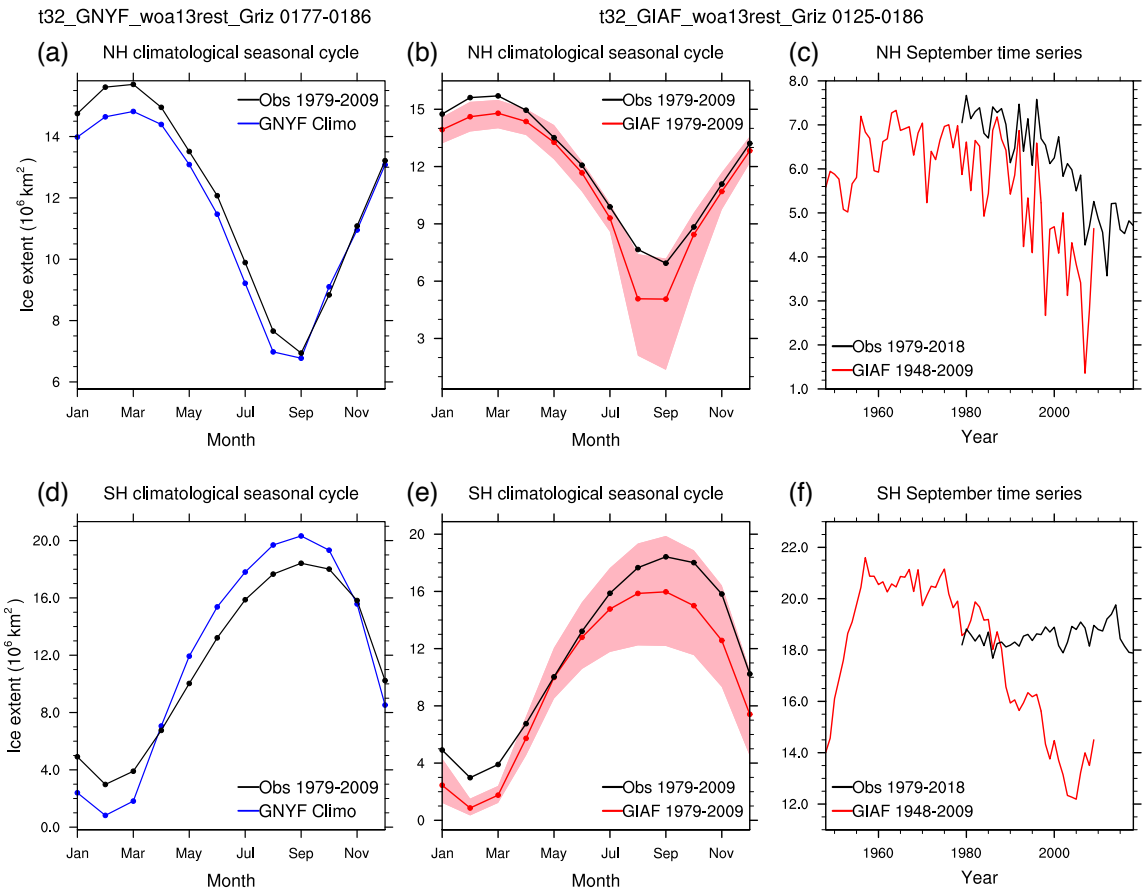

Figure 14: Climatological seasonal cycle of the sea ice extent of **(a)** GNYF and **(b)** GIAF in the Northern Hemisphere, compared with satellite passive microwave-derived data sets (Sea Ice Index, version 3; *Fetterer et al.*, 2017). In **(b)**, red indicates model period corresponding to the observational period, with shadow indicating the maximum and minimum envelope. **(c)** Time series of the September sea ice area of GIAF compared with the satellite data. **(d to f)** Same as **(a to c)**, but for the Southern Hemisphere. The sea ice extent is calculated as the model grid area with an ice concentration of 15% or more.

the August concentration is roughly equal to the September in GIAF (Fig. 14a and b). The March concentrations are 14.82 million km^2 in GNYF and 14.79 million km^2 in GIAF, both lower than the observational value of 15.70 million km^2. This is consistent with the concentration map (Figure 13), which shows that it is mostly due to the missing ice over the Greenland Sea, Labrador Sea, and Sea of Okhotsk. The September concentration in GNYF is remarkably consistent with the observation (6.94 million km^2), while that in GIAF is lower (5.06 million km^2) with a wide envelope. Although its September sea ice has a lower mean, a higher standard deviation, and a stronger decreasing trend, CICE5 in HiLAT03 has an improved summer sea ice representation than the previous CICE4 in the NCAR 1° model (Fig. 14c; Table 3), in these statistics.

In the Southern Hemisphere, the timing of the maximum and minimum occurrence of the sea ice extent in HiLAT03 is consistent with the observation (Fig. 14d and e). The February

extent in GNYF and GIAF are similar with values of 0.82 and 0.86 million km^2, respectively, both lower than the observation (2.98 million km^2). But the September extent in these two experiments are different, with GNYF being higher than the observation (20.32 vs. 18.42 million km^2) and GIAF being lower than the observation. The different behaviors between these two cases is due to the strong Weddell Sea deep convection, which is clear in the last few decades of the September time series (Fig. 14f). In general, HiLAT03 has a stronger seasonal cycle of ice extent in the Southern Hemisphere, being without the prolonged Weddell-Sea polynya.

4.2 Sea ice thickness and volume

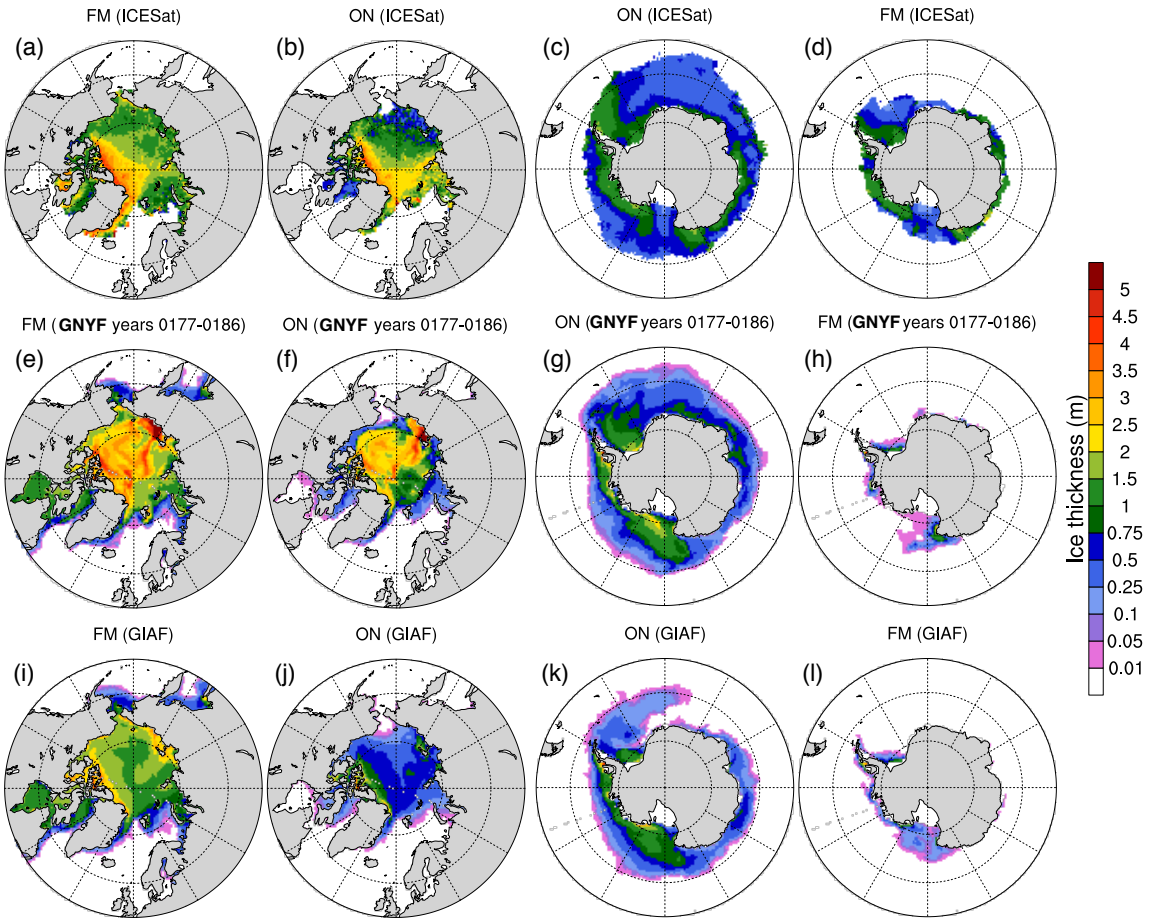

Figure 15: Climatological spring and fall sea ice thickness (m) of **(a–d)** ICESat data (*Kwok et al.*, 2009), **(e–h)** GNYF, and **(i–l)** GIAF in the (left) Northern and (right) Southern Hemispheres. The ICESat data are averaged over spring 2004–2008 and fall 2003–2007, and same for the GIAF case. The GNYF follows the previous convention, which uses the average over the last 10 years. In the Northern Hemisphere, spring and fall are defined as February–March and October–November, respectively, and vice versa in the Southern Hemisphere. Note the colormap is non-linear with smaller increments over the low-value range.

Spring and fall sea ice thicknesses. Large-scale gridded ice thickness data set is hard to established, but short-term satellite-based retrievals of ice thickness using RADAR or LIDAR altimeters (*Giles et al.*, 2008; *Kwok et al.*, 2009) have become available, although the retrieval techniques are subject to a variety of errors. Here the sea ice thickness is assessed in Figure 15 by gridded observations derived from Ice, Cloud and Land Elevation Satellite (ICESat) measurements during the 5-year period of 2003/04–2007/08 (*Kwok et al.*, 2009). In the Northern Hemisphere, a general impression is that the GNYF case captures the values well but not the pattern, while the GIAF case does the opposite. ICESat shows very thick ice (> 4 m) north of Greenland and the Canadian Arctic Archipelago (CAA) in both spring and fall, and the fall thinning occurs mostly over the Bering Strait side of the Arctic Ocean. In GNYF, very thick ice occurs in many regions across the Arctic; not only north of Greenland and the CAA but also central Arctic and the Eurasian shelf seas. In GIAF, the spring ice shows thick ice along two sides of the Arctic: both the CAA-Greenland side and the Eurasian-shelf side. The fall ice, instead, resembles the pattern well but with systematically lower values (< 0.75 m).

In the Southern Hemisphere, the GNYF case generally captures the spring (ON) pattern, except that the thickness outside of the Ross Sea is overestimated, while the GIAF misrepresent the ice over the Indian Ocean sector, consistent with the low ice concentration found over this region during winter time (Fig. 13k). None of them is able to represent the thick ice (> 0.75 m) close to the Antarctica in the fall (FM) season.

Seasonal cycle of ice volume. The sea ice volume depends on both the sea ice area and thickness, and typically has a large spread between models (*Wang et al.*, 2016a). Here we first form the product of monthly ice area and ice thickness with an ice concentration of 15% or more for each grid cell, then sum for each hemisphere, and finally average over time to get the seasonal cycle of ice volume (Fig. 16). We compare the Northern Hemisphere ice volume with the Pan-Arctic Ice Ocean Modeling and Assimilation System (PIOMAS) reanalysis data (*Schweiger et al.*, 2011).

In the Northern Hemisphere, the seasonal cycle of the GNYF case is remarkably consistent with the PIOMAS reanalysis (Fig. 16a), with maximum at April (28.34 10^3 km^3) and minimum at September (11.00 10^3 km^3). The maximum ice volume (April) lags the maximum ice extent (March) by one month, indicating that the ice thickness maximizes at April instead of March and is more dominant in determining the winter-time ice volume. However, the seasonal cycle of the GIAF case is systematically lower than the PIOMAS reanalysis by about 5–8 10^3 km^3 (Fig. 16b). The volume mismatch is mostly due to the ice thickness instead of ice extent, since the mismatch of sea ice extent between two cases is small, and the ice thickness maps seem quite different between two cases (Fig. 15, e and f vs. i and j). The ice thickness mismatch between the two cases could be due to 1) the atmospheric forcing, where the atmospheric conditions are essentially the same data set except that one is the climatology and the other includes inter-annual variability, 2) different ocean circulations and surface conditions corresponding to different atmospheric forcing, 3)

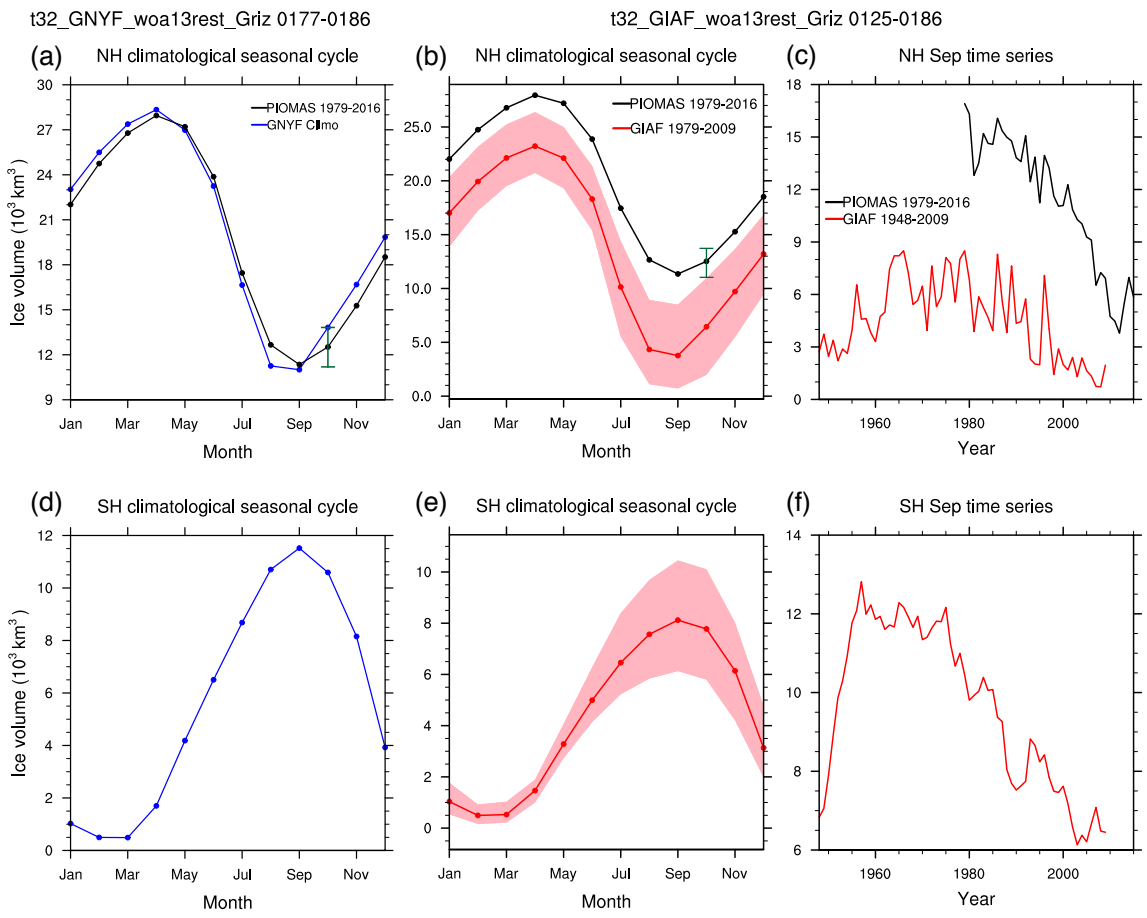

Figure 16: Similar as Figure 14, but for the sea ice volume. The model results in the Northern Hemisphere are compared with PIOMAS Arctic sea ice volume reanalysis of 1979–2016 (*Schweiger et al.*, 2011). The green error bars in **a** and **b** represent the estimated October total ice volume uncertainty of ± 1.35 10^3 km^3 in PIOMAS. The sea ice volume is calculated as the product of ice area and ice thickness with an ice concentration of 15% or more.

the export of multiyear ice being transported out during the last 30 years in the GIAF case but not in the GNYF case, or 4) some combination of these effects. Due to the fact that the September ice volume of GIAF is overall 7.58 10^3 km^3 lower than the reanalysis, it is hard for GIAF to simulate the dramatic decline during the 1979–2016 period as in the reanalysis (Fig. 16c).

In the Southern Hemisphere, the GNYF ice volume in February and March are similar (0.50 10^3 km^3 and 0.49 10^3 km^3, respectively) and both are considered as the minimum during the seasonal cycle (Fig. 16d). Considering the ice extent minimized in February, such similar values indicate that ice thickness minimizes in March. The seasonal cycle peaks in September (11.52 10^3 km^3), consistent with the peak of the ice extent. By contrast, the peak value in the GIAF case is much lower with a mean of 8.12 10^3 km^3, which is mostly due to the Weddell-Sea deep convection as discussed before (Fig. 16f).

5 Summary and Discussion

We have described the parameterization setups of the ocean and sea ice components of the E3SMv0-HiLAT climate model in the HiLAT03 configuration. The purpose of configuring the HiLAT03 model as a descendant of the 1° ocean and sea ice components of E3SMv0-HiLAT is 1) to better represent the ocean bathymetry at high latitudes with increased horizontal and vertical resolutions, 2) to explicitly resolve small-scale processes such as mesoscale eddies (eddy-permitting), and 3) to allow for long-term simulations. We choose not to use an explicit lateral diffusion (no eddy parameterization), and choose to use a non-dispersive advective scheme accordingly. This model will be used to study regional ocean/sea ice climates which potentially have global climate impacts. One example could be the Agulhas leakage, which transports warm and salty water from the Indian Ocean to the South Atlantic through large-size eddies (Agulhas Rings), alters the Atlantic salinity distribution, and potentially affects the AMOC. Another example is the Arctic freshwater content, which could be transported to the North Atlantic deep water formation regions and change the AMOC. It requires good representation of the ocean bathymetry over the Canadian Arctic Archipelago, as well as transport pathways such as the Nares, Davis, and Fram Straits.

We provided an overview of the salient features of the ocean and sea ice climate in two CORE-forced control simulations in comparison with available observations. The model simulates reasonable surface temperature and salinity fields, but with a subsurface warm bias in general. Such a warm bias is likely due to the absent of the upward heat transport by the unrepresented mesoscale eddies, especially at high latitudes, which is supposed to balance the downward heat transport by mean flow. The SSH variability in HiLAT03 exhibits similar geographical distributions of variability and differs primarily in amplitude when compared with observation, as expected, but has a surprisingly decent representation at the Argentine Basin and the Agulhas leakage region. The winter and summer MLDs agree well in the overall distribution patterns with observation, but produces deeper MLDs at the deep water formation regions as found in other FOSI simulations. HiLAT03 produces reasonable horizontal general circulations, with indexes at the North Atlantic falling in the middle of the multi-model range of the FOSI simulations. The meridional overturning circulations in HiLAT03 is slightly smaller than the observations, especially in the inter-annually forced case. The meridional heat transport is satisfactory at most latitudes of the globe without explicit eddy parameterization. One implication is that heat transport in eddy-resolving or eddy-permitting models is accomplished by standing eddies (meanders), such as the ACC in the Southern Ocean and the Gulf Stream in the mid-latitude North Atlantic, not by transient eddies. In GM-parameterized models, the heat fluxes by the parameterized eddies are dominant (*Hecht et al.*, 2019a). A prolonged deep convection over the Weddell Sea and the Indian Ocean sector of the Southern Ocean is found in the inter-annually forced case, which imposes both local and remote impacts. We discussed possibilities of the cause and suspect the surface salinity restoring might be the trigger.

The new sea ice model, CICE5 in HiLAT03, differs significantly from its predecessor

CICE4 used in the 1° NCAR model in physical processes, parameter combination and horizontal resolution. The Arctic sea ice in HiLAT03 improves both in extent and thickness. But similar to the 1° NCAR model, the Antarctic summer sea ice in HiLAT03 is still underrepresented, both in extent and thickness, compared with the observation.

One interesting feature shown in the depth-dependent ocean temperature drift is that the top-to-bottom warming drift pattern, as shown and discussed in Figure 4, is quite different from results in coupled models. An overall cooling trend is found in a 1850-control simulation of CCSM4 with a 1° POP2 with the magnitude of −0.4°C, reflecting the heat loss at the top of atmosphere in the coupled system (*Danabasoglu et al.*, 2012). However, a pattern of cooling in the upper 500 m and warming below this depth has been found in 1850-control simulations using more recent CCSM/CESM versions, such as CESM1 (*Kay et al.*, 2015) and E3SMv0-HiLAT (*Hecht et al.*, 2019b) with 1° POP2. It is so far unclear why such an upper-cooling-lower-warming drift occurs in the latter case. In fact, this upper-cooling-lower-warming drift is common in modern control simulations, such as the GFDL models (CM2.1, CM2.5, and CM2.6; *Delworth et al.*, 2012; *Griffies et al.*, 2015) and the HadGEM3 models (GC3.1; *Kuhlbrodt et al.*, 2018). This type of drift is expected in the modern controls because a net ocean heat uptake occurs in these models due to a positive downward heat flux crossing the ocean surface, and is enhanced either by an overly dominant mean flow or too weak mesoscale eddy field (*Griffies et al.*, 2015). But it is unexpected in 1850 controls, since a net radiative cooling effect is applied to an ocean state initiated from modern observations. At least, our results show that the ocean model itself responds reasonably to external forcing in term of heat loss/update, and the unexpected cooling in 1850 controls (*Kay et al.*, 2015; *Hecht et al.*, 2019b) are likely due to atmospheric adjustments which reverses the sign of the ocean surface heat flux.

Another interesting feature of the ocean component is that in the Atlantic, the AABW formation in the south seems to be negatively correlated with the NADW formation in the north. That is, a significant increase in AABW formation by ∼10 Sv (related to the prolonged polynya) could induce a decrease of NADW formation by about 2–4 Sv in the GIAF case, as shown in the AMOC time series (Fig. 10). According to many ocean modeling studies (*Mecking et al.*, 2016; *Zhang et al.*, 2017) and paleocean observations (*Skinner et al.*, 2014), an oscillatory behavior of the AABW and NADW formations may be an important indicator for the AMOC to fall in a bi-stable mode. The low resolution POP2 in previous versions of CCSM/CESM has been reported to be mono-stable and a hysteresis behavior is lacking (*Liu et al.*, 2009; *Bryan et al.*, 2006; *Meehl et al.*, 2012, 2013). In those simulations, the AABW (as well as Antarctic Intermediate Water, AAIW) has been reported to be positively correlated with the NADW formation (*Zhang et al.*, 2017; *Gu et al.*, 2017). If the oscillatory behavior of AABW and NADW is indeed a indicator for a bi-stable AMOC, it implies that the current configuration of POP2 at eddy-permitting resolution of the POP2 could have a different AMOC stability from its low-resolution predecessors. Further detailed studies of long-term, coupled simulations, which are beyond the purposes of this report, will be helpful to explore whether the AMOC stability in POP2 is resolution dependent.

In this report we focused on describing the global, large-scale performance of HiLAT03. An Arctic-focused model description and evaluation is presented elsewhere. Detailed comparison with the 1° FOSI simulation of the E3SMv0-HiLAT model (HiLAT10) and analyses of the reasons for the differences across resolutions will be the subject of future investigations.

Acknowledgements

This research was supported by the Regional and Global Model Analysis (RGMA) component of the Earth and Environmental System Modeling (EESM) program of the U.S. Department of Energy's Office of Science, as contribution to the HiLAT-RASM project. The computations were done on the Institutional Computing facilities at Los Alamos National Laboratory.

References

Abram, N. J., R. Mulvaney, E. W. Wolff, J. Triest, S. Kipfstuhl, L. D. Trusel, F. Vimeux, L. Fleet, and C. Arrowsmith, Acceleration of snow melt in an Antarctic Peninsula ice core during the twentieth century, *Nat. Geosci.*, *6*(5), 404–411, doi:10.1038/ngeo1787, 2013.

Adcroft, A., C. Hill, and J. Marshall, Representation of topography by shaved cells in a height coordinate ocean model, *Mon. Weather Rev.*, *125*(9), 2293–2315, doi:10.1175/1520-0493(1997)125⟨2293:ROTBSC⟩2.0.CO;2, 1997.

Biastoch, A., C. W. Böning, and J. R. E. Lutjeharms, Agulhas leakage dynamics affects decadal variability in Atlantic overturning circulation, *Nature*, *456*(7221), 489–492, doi:10.1038/nature07426, 2008.

Boyer, T., et al., *World Ocean Database 2013*, 208 pp., NOAA Printing Office, Silver Spring, MD, doi:10.7289/V5NZ85MT, 2013.

Bryan, F. O., and R. D. Smith, Modelling the North Atlantic circulation: from eddy-permitting to eddy-resolving, *Int. WOCE Newsl.*, *33*, 12–14, 1998.

Bryan, F. O., G. Danabasoglu, N. Nakashiki, Y. Yoshida, D.-H. Kim, J. Tsutsui, and S. C. Doney, Response of the North Atlantic Thermohaline Circulation and ventilation to increasing carbon dioxide in CCSM3, *J. Clim.*, *19*(11), 2382–2397, doi:10.1175/JCLI3757.1, 2006.

Carmack, E. C., et al., Toward Quantifying the Increasing Role of Oceanic Heat in Sea Ice Loss in the New Arctic, *Bull. Am. Meteorol. Soc.*, *96*(12), 2079–2105, doi:10.1175/BAMS-D-13-00177.1, 2015.

Carsey, F. D., Microwave observation of the Weddell polynya, *Mon. Weather Rev.*, *108*(12), 2032–2044, doi:10.1175/1520-0493(1980)108⟨2032:MOOTWP⟩2.0.CO;2, 1980.

Cassano, J. J., et al., Development of the Regional Arctic System Model (RASM): Near-surface atmospheric climate sensitivity, *J. Clim.*, *30*(15), 5729–5753, doi:10.1175/JCLI-D-15-0775.1, 2017.

Cavalieri, D. J., C. L. Parkinson, P. Gloersen, and H. J. Zwally, Sea ice concentrations from Nimbus-7 SMMR and DMSP SSM/I-SSMIS passive microwave data, version 1, doi:10.5067/8GQ8LZQVL0VL, 1999.

Cheon, W. G., S.-K. Lee, A. L. Gordon, Y. Liu, C.-B. Cho, and J. J. Park, Replicating the 1970s' Weddell Polynya using a coupled ocean-sea ice model with reanalysis surface flux fields, *Geophys. Res. Lett.*, *42*(13), 5411–5418, doi:10.1002/2015GL064364, 2015.

Comiso, J. C., and F. Nishio, Trends in the sea ice cover using enhanced and compatible AMSR-E, SSM/I, and SMMR data, *J. Geophys. Res.*, *113*(C2), C02S07, doi:10.1029/2007JC004257, 2008.

Comiso, J. C., C. L. Parkinson, R. Gersten, and L. Stock, Accelerated decline in the Arctic sea ice cover, *Geophys. Res. Lett.*, *35*(1), L01,703, doi:10.1029/2007GL031972, 2008.

Danabasoglu, G., S. C. Bates, B. P. Briegleb, S. R. Jayne, M. Jochum, W. G. Large, S. Peacock, and S. G. Yeager, The CCSM4 ocean component, *J. Clim.*, *25*(5), 1361–1389, doi:10.1175/JCLI-D-11-00091.1, 2012.

Danabasoglu, G., et al., North Atlantic simulations in Coordinated Ocean-ice Reference Experiments phase II (CORE-II). Part I: Mean states, *Ocean Model.*, *73*, 76–107, doi:10.1016/j.ocemod.2013.10.005, 2014.

Danabasoglu, G., et al., North Atlantic simulations in Coordinated Ocean-ice Reference Experiments phase II (CORE-II). Part II: Inter-annual to decadal variability, *Ocean Model.*, *97*, 65–90, doi:10.1016/j.ocemod.2015.11.007, 2016.

Delworth, T. L., et al., Simulated climate and climate change in the GFDL CM2.5 high-resolution coupled climate model, *J. Clim.*, *25*(8), 2755–2781, doi:10.1175/JCLI-D-11-00316.1, 2012.

Downes, S. M., et al., An assessment of Southern Ocean water masses and sea ice during 1988-2007 in a suite of interannual CORE-II simulations, *Ocean Model.*, *94*, 67–94, doi:10.1016/j.ocemod.2015.07.022, 2015.

Ducet, N., P. Y. Le Traon, and G. Reverdin, Global high-resolution mapping of ocean circulation from TOPEX/Poseidon and ERS-1 and -2, *J. Geophys. Res. Ocean.*, *105*(C8), 19,477–19,498, doi:10.1029/2000JC900063, 2000.

Eyring, V., S. Bony, G. A. Meehl, C. A. Senior, B. Stevens, R. J. Stouffer, and K. E. Taylor, Overview of the Coupled Model Intercomparison Project Phase 6 (CMIP6) experimental design and organization, *Geosci. Model Dev.*, *9*(5), 1937–1958, doi:10.5194/gmd-9-1937-2016, 2016.

Fanning, A. F., and A. J. Weaver, A horizontal resolution and parameter sensitivity study of heat transport in an idealized coupled climate model, *J. Clim.*, *10*(10), 2469–2478, doi:10.1175/1520-0442(1997)010⟨2469:AHRAPS⟩2.0.CO;2, 1997.

Fetterer, F., K. Knowles, W. N. Meier, M. Savoie, and A. K. Windnagel, Sea Ice Index, Version 3., doi:10.7265/N5K072F8, 2017.

Fox-Kemper, B., and D. Menemenlis, Can large eddy simulation techniques improve mesoscale rich ocean models?, in *Ocean Model. an Eddying Regime*, edited by M. W. Hecht and H. Hasumi, pp. 319–337, American Geophysical Union, doi:10.1029/177GM19, 2008.

Ganachaud, A., and C. Wunsch, Large-Scale Ocean Heat and Freshwater Transports during the World Ocean Circulation Experiment, *J. Clim.*, *16*(4), 696–705, doi:10.1175/1520-0442(2003)016⟨0696:LSOHAF⟩2.0.CO;2, 2003.

Gary, S. F., M. Susan Lozier, C. W. Böning, and A. Biastoch, Deciphering the pathways for the deep limb of the Meridional Overturning Circulation, *Deep Sea Res. Part II Top. Stud. Oceanogr.*, *58*(17-18), 1781–1797, doi:10.1016/j.dsr2.2010.10.059, 2011.

Gent, P., F. Bryan, S. Doney, and W. Large, A perspective on the ocean component of climate models, *CLIVAR Exch.*, *4*(4), 11–14, 1999.

Gent, P. R., and J. C. Mcwilliams, Isopycnal mixing in ocean circulation models, *J. Phys. Oceanogr.*, *20*(1), 150–155, doi:10.1175/1520-0485(1990)020⟨0150:IMIOCM⟩2.0.CO;2, 1990.

Giles, K. A., S. W. Laxon, and A. L. Ridout, Circumpolar thinning of Arctic sea ice following the 2007 record ice extent minimum, *Geophys. Res. Lett.*, *35*(22), L22,502, doi:10.1029/2008GL035710, 2008.

Griffies, S. M., M. Winton, B. Samuels, G. Danabasoglu, S. Yeager, S. Marsland, H. Drange, and M. Bentsen, Datasets and protocol for the CLIVAR WGOMD Coordinated Ocean-sea ice Reference Experiments (COREs), *Tech. rep.*, WCRP Report No. 21/2012, 2012.

Griffies, S. M., et al., Coordinated Ocean-ice Reference Experiments (COREs), *Ocean Model.*, *26*(1-2), 1–46, doi:10.1016/j.ocemod.2008.08.007, 2009.

Griffies, S. M., et al., Impacts on Ocean Heat from Transient Mesoscale Eddies in a Hierarchy of Climate Models, *J. Clim.*, *28*(3), 952–977, doi:10.1175/JCLI-D-14-00353.1, 2015.

Gu, S., Z. Liu, J. Zhang, J. Rempfer, F. Joos, and D. W. Oppo, Coherent Response of Antarctic Intermediate Water and Atlantic Meridional Overturning Circulation During the Last Deglaciation: Reconciling Contrasting Neodymium Isotope Reconstructions From the Tropical Atlantic, *Paleoceanography*, *32*(10), 1036–1053, doi:10.1002/2017PA003092, 2017.

Hallberg, R., Using a resolution function to regulate parameterizations of oceanic mesoscale eddy effects, *Ocean Model.*, *72*, 92–103, doi:10.1016/j.ocemod.2013.08.007, 2013.

Hecht, M., W. Weijer, G. Vallis, and C. Dawson, Partitioning of Southern Ocean heat transport between transient and standing eddies: Insight from an idealized multi-resolution study, in review, 2019a.

Hecht, M., et al., E3SMv0-HiLAT : A modified climate system model targeted for the study of high latitude processes, in review, 2019b.

Hecht, M. W., and H. Hasumi, *Ocean Modeling in an Eddying Regime*, *Geophysical Monograph Series*, vol. 177, American Geophysical Union, Washington, D. C., doi:10.1029/GM177, 2008.

Hirabara, M., H. Tsujino, H. Nakano, and G. Yamanaka, Formation mechanism of the Weddell Sea Polynya and the impact on the global abyssal ocean, *J. Oceanogr.*, *68*(5), 771–796, doi:10.1007/s10872-012-0139-3, 2012.

Holte, J., L. D. Talley, J. Gilson, and D. Roemmich, An Argo mixed layer climatology and database, *Geophys. Res. Lett.*, *44*(11), 5618–5626, doi:10.1002/2017GL073426, 2017.

Hunke, E. C., and J. K. Dukowicz, An elastic-viscous-plastic model for sea ice dynamics, *J. Phys. Oceanogr.*, *27*(9), 1849–1867, doi:10.1175/1520-0485(1997)027⟨1849:AEVPMF⟩2.0.CO;2, 1997.

Hunke, E. C., D. A. Hebert, and O. Lecomte, Level-ice melt ponds in the Los Alamos sea ice model, CICE, *Ocean Model.*, *71*, 26–42, doi:10.1016/j.ocemod.2012.11.008, 2013.

Hunke, E. C., W. H. Lipscomb, A. K. Turner, N. Jeffery, and S. Elliott, CICE : The Los Alamos Sea Ice Model documentation and software user's manual version 5.1 (LA-CC-06-012), *Tech. rep.*, Los Alamos National Laboratory, 2015.

Hurrell, J. W., et al., The Community Earth System Model: A framework for collaborative research, *Bull. Am. Meteorol. Soc.*, *94*(9), 1339–1360, doi:10.1175/BAMS-D-12-00121.1, 2013.

Jahn, A., et al., Late-twentieth-century simulation of arctic sea ice and ocean properties in the CCSM4, *J. Clim.*, *25*(5), 1431–1452, doi:10.1175/JCLI-D-11-00201.1, 2012.

Jansen, M. F., I. M. Held, A. Adcroft, and R. Hallberg, Energy budget-based backscatter in an eddy permitting primitive equation model, *Ocean Model.*, *94*, 15–26, doi:10.1016/j.ocemod.2015.07.015, 2015.

Kay, J. E., et al., The Community Earth System Model (CESM) large ensemble project: A community resource for studying climate change in the presence of internal climate variability, *Bull. Am. Meteorol. Soc.*, *96*(8), 1333–1349, doi:10.1175/BAMS-D-13-00255.1, 2015.

Kuhlbrodt, T., et al., The low-resolution version of HadGEM3 GC3.1: Development and evaluation for global climate, *J. Adv. Model. Earth Syst.*, *10*(11), 2865–2888, doi:10.1029/2018MS001370, 2018.

Kurtakoti, P., M. Veneziani, A. Stössel, and W. Weijer, Preconditioning and formation of Maud Rise polynyas in a high-resolution Earth System Model, *J. Clim.*, *31*(23), 9659–9678, doi:10.1175/JCLI-D-18-0392.1, 2018.

Kwok, R., G. F. Cunningham, M. Wensnahan, I. Rigor, H. J. Zwally, and D. Yi, Thinning and volume loss of the Arctic Ocean sea ice cover: 2003-2008, *J. Geophys. Res.*, *114*(C7), C07,005, doi:10.1029/2009JC005312, 2009.

Large, W. G., and S. G. Yeager, The global climatology of an interannually varying airsea flux data set, *Clim. Dyn.*, *33*(2-3), 341–364, doi:10.1007/s00382-008-0441-3, 2009.

Large, W. G., J. C. McWilliams, and S. C. Doney, Oceanic vertical mixing: A review and a model with a nonlocal boundary layer parameterization, *Rev. Geophys.*, *32*(4), 363–403, doi:10.1029/94RG01872, 1994.

Large, W. G., G. Danabasoglu, J. C. McWilliams, P. R. Gent, and F. O. Bryan, Equatorial circulation of a global ocean climate model with anisotropic horizontal viscosity, *J. Phys. Oceanogr.*, *31*(2), 518–536, doi:10.1175/1520-0485(2001)031⟨0518:ECOAGO⟩2.0.CO;2, 2001.

Leonard, B. P., A stable and accurate convective modelling procedure based on quadratic upstream interpolation, *Comput. Methods Appl. Mech. Eng.*, *19*(1), 59–98, doi:10.1016/0045-7825(79)90034-3, 1979.

Levitus, S., M. Conkright, T. Boyer, T. O'Brien, J. Antonov, C. Stephens, L. Stathoplos, D. Johnson, and R. Gelfeld, *World Ocean Database 1998, Volume 1: Introduction*, 346 pp., U.S. Gov. Printing Office, Wash., D.C., 1998.

Liu, H., X. Zhang, W. Li, Y. Yu, and R. Yu, An eddy-permitting oceanic general circulation model and its preliminary evaluation, *Adv. Atmos. Sci.*, *21*(5), 675–690, doi:10.1007/BF02916365, 2004.

Liu, Z., et al., Transient simulation of last deglaciation with a new mechanism for Bølling-Allerød warming, *Science*, *325*(5938), 310–314, doi:10.1126/science.1171041, 2009.

Lozier, M. S., et al., A sea change in our view of overturning in the subpolar North Atlantic, *Science*, *363*(6426), 516–521, doi:10.1126/science.aau6592, 2019.

Madec, G., and the NEMO Team, *NEMO ocean engine*, 27, 1–386 pp., Institut Pierre-Simon Laplace (IPSL), France, 2016.

Maltrud, M., and G. Holloway, Implementing biharmonic neptune in a global eddying ocean model, *Ocean Model.*, *21*(1-2), 22–34, doi:10.1016/j.ocemod.2007.11.003, 2008.

Maslowski, W., J. Clement Kinney, M. Higgins, and A. Roberts, The Future of Arctic Sea Ice, *Annu. Rev. Earth Planet. Sci.*, *40*(1), 625–654, doi:10.1146/annurev-earth-042711-105345, 2012.

Mazloff, M. R., P. Heimbach, and C. Wunsch, An eddy-permitting Southern Ocean state estimate, *J. Phys. Oceanogr.*, *40*(5), 880–899, doi:10.1175/2009JPO4236.1, 2010.

Mecking, J., S. Drijfhout, L. Jackson, and M. Andrews, The effect of model bias on Atlantic freshwater transport and implications for AMOC bi-stability, *Tellus A Dyn. Meteorol. Oceanogr.*, *69*(1), 1299,910, doi:10.1080/16000870.2017.1299910, 2017.

Mecking, J. V., S. S. Drijfhout, L. C. Jackson, and T. Graham, Stable AMOC off state in an eddy-permitting coupled climate model, *Clim. Dyn.*, *47*(7-8), 2455–2470, doi:10.1007/s00382-016-2975-0, 2016.

Meehl, G. A., et al., Climate system response to external forcings and climate change projections in CCSM4, *J. Clim.*, *25*(11), 3661–3683, doi:10.1175/JCLI-D-11-00240.1, 2012.

Meehl, G. A., et al., Climate change projections in CESM1(CAM5) compared to CCSM4, *J. Clim.*, *26*(17), 6287–6308, doi:10.1175/JCLI-D-12-00572.1, 2013.

Murray, R. J., Explicit generation of orthogonal grids for ocean models, *J. Comput. Phys.*, *126*(2), 251–273, doi:10.1006/jcph.1996.0136, 1996.

Newman, M., G. P. Compo, and M. A. Alexander, ENSO-forced variability of the Pacific Decadal Oscillation, *J. Clim.*, *16*(23), 3853–3857, doi:10.1175/1520-0442(2003)016⟨3853:EVOTPD⟩2.0.CO;2, 2003.

Olson, D. B., and R. H. Evans, Rings of the Agulhas current, *Deep Sea Res. Part A. Oceanogr. Res. Pap.*, *33*(1), 27–42, doi:10.1016/0198-0149(86)90106-8, 1986.

Parkinson, C. L., D. J. Cavalieri, P. Gloersen, H. J. Zwally, and J. C. Comiso, Arctic sea ice extents, areas, and trends, 1978-1996, *J. Geophys. Res. Ocean.*, *104*(C9), 20,837–20,856, doi:10.1029/1999JC900082, 1999.

Pichevin, T., D. Nof, and J. Lutjeharms, Why Are There Agulhas Rings?, *J. Phys. Oceanogr.*, *29*(4), 693–707, doi:10.1175/1520-0485(1999)029⟨0693:WATAR⟩2.0.CO;2, 1999.

Pickart, R. S., and M. A. Spall, Impact of Labrador Sea convection on the North Atlantic Meridional Overturning Circulation, *J. Phys. Oceanogr.*, *37*(9), 2207–2227, doi:10.1175/JPO3178.1, 2007.

Roberts, A., A. Craig, W. Maslowski, R. Osinski, A. Duvivier, M. Hughes, B. Nijssen, J. Cassano, and M. Brunke, Simulating transient ice-ocean Ekman transport in the Regional Arctic System Model and Community Earth System Model, *Ann. Glaciol.*, *56*(69), 211–228, doi:10.3189/2015AoG69A760, 2015.

Rothstein, L., et al., Modeling Ocean Ecosystems: The PARADIGM Program, *Oceanography*, *19*(1), 22–51, doi:10.5670/oceanog.2006.89, 2006.

Schweiger, A., R. Lindsay, J. Zhang, M. Steele, H. Stern, and R. Kwok, Uncertainty in modeled Arctic sea ice volume, *J. Geophys. Res.*, *116*, C00D06, doi:10.1029/2011JC007084, 2011.

Sidorenko, D., et al., Towards multi-resolution global climate modeling with ECHAM6-FESOM. Part I: Model formulation and mean climate, *Clim. Dyn.*, *44*(3-4), 757–780, doi:10.1007/s00382-014-2290-6, 2015.

Skinner, L. C., C. Waelbroeck, A. E. Scrivner, and S. J. Fallon, Radiocarbon evidence for alternating northern and southern sources of ventilation of the deep Atlantic carbon pool during the last deglaciation, *Proc. Natl. Acad. Sci.*, *111*(15), 5480–5484, doi:10.1073/pnas.1400668111, 2014.

Small, R. J., et al., A new synoptic scale resolving global climate simulation using the Community Earth System Model, *J. Adv. Model. Earth Syst.*, *6*(4), 1065–1094, doi:10.1002/2014MS000363, 2014.

Smedsrud, L. H., A. Sirevaag, K. Kloster, A. Sorteberg, and S. Sandven, Recent wind driven high sea ice area export in the Fram Strait contributes to Arctic sea ice decline, *Cryosph.*, *5*(4), 821–829, doi:10.5194/tc-5-821-2011, 2011.

Smeed, D., G. McCarthy, D. Rayner, B. I. Moat, W. E. Johns, M. O. Baringer, and C. S. Meinen, Atlantic meridional overturning circulation observed by the RAPID-MOCHA-WBTS (RAPID-Meridional Overturning Circulation and Heatflux Array-Western Boundary Time Series) array at 26N from 2004 to 2017., *Tech. rep.*, British Oceanographic Data Centre - Natural Environment Research Council, UK., doi:10.5285/5acfd143-1104-7b58-e053-6c86abc0d94b, 2017.

Smith, R., et al., The Parallel Ocean Program (POP) reference manual: Ocean component of the Community Climate System Model (CCSM), *Tech. rep.*, Los Alamos National Laboratory, 2010.

Smith, R. D., M. E. Maltrud, F. O. Bryan, and M. W. Hecht, Numerical simulation of the North Atlantic Ocean at 1/10, *J. Phys. Oceanogr.*, *30*(7), 1532–1561, doi:10.1175/1520-0485(2000)030⟨1532:NSOTNA⟩2.0.CO;2, 2000.

Spence, J. P., M. Eby, and A. J. Weaver, The sensitivity of the Atlantic Meridional Overturning Circulation to freshwater forcing at eddy-permitting resolutions, *J. Clim.*, *21*(11), 2697–2710, doi:10.1175/2007JCLI2103.1, 2008.

Steele, M., R. Morley, and W. Ermold, PHC: A global ocean hydrography with a high-quality Arctic Ocean, *J. Clim.*, *14*(9), 2079–2087, doi:10.1175/1520-0442(2001)014⟨2079:PAGOHW⟩2.0.CO;2, 2001.

Steele, M., J. Zhang, and W. Ermold, Mechanisms of summertime upper Arctic Ocean warming and the effect on sea ice melt, *J. Geophys. Res.*, *115*(C11), C11,004, doi:10.1029/2009JC005849, 2010.

Stössel, A., Z. Zhang, and T. Vihma, The effect of alternative real-time wind forcing on Southern Ocean sea ice simulations, *J. Geophys. Res.*, *116*(C11), C11,021, doi:10.1029/2011JC007328, 2011.

Stroeve, J., M. Serreze, S. Drobot, S. Gearheard, M. Holland, J. Maslanik, W. Meier, and T. Scambos, Arctic Sea Ice Extent Plummets in 2007, *Eos, Trans. Am. Geophys. Union*, *89*(2), 13, doi:10.1029/2008EO020001, 2008.

Trenberth, K. E., and J. M. Caron, Estimates of meridional atmosphere and ocean heat transports, *J. Clim.*, *14*(16), 3433–3443, doi:10.1175/1520-0442(2001)014⟨3433:EOMAAO⟩2.0.CO;2, 2001.

Turner, A. K., and E. C. Hunke, Impacts of a mushy-layer thermodynamic approach in global sea-ice simulations using the CICE sea-ice model, *J. Geophys. Res. Ocean.*, *120*(2), 1253–1275, doi:10.1002/2014JC010358, 2015.

Urrego-Blanco, J. R., N. M. Urban, E. C. Hunke, A. K. Turner, and N. Jeffery, Uncertainty quantification and global sensitivity analysis of the Los Alamos sea ice model, *J. Geophys. Res. Ocean.*, *121*(4), 2709–2732, doi:10.1002/2015JC011558, 2016.

Urrego-Blanco, J. R., E. C. Hunke, N. M. Urban, N. Jeffery, A. K. Turner, J. R. Langenbrunner, and J. M. Booker, Validation of sea ice models using an uncertainty-based distance metric for multiple model variables, *J. Geophys. Res. Ocean.*, *122*(4), 2923–2944, doi:10.1002/2016JC012602, 2017.

Wang, Q., et al., An assessment of the Arctic Ocean in a suite of interannual CORE-II simulations. Part I: Sea ice and solid freshwater, *Ocean Model.*, *99*, 110–132, doi:10.1016/j.ocemod.2015.12.008, 2016a.

Wang, Q., et al., An assessment of the Arctic Ocean in a suite of interannual CORE-II simulations. Part II: Liquid freshwater, *Ocean Model.*, *99*, 86–109, doi:10.1016/j.ocemod.2015.12.009, 2016b.

Waterman, S., N. G. Hogg, and S. R. Jayne, Eddy-mean flow interaction in the Kuroshio Extension region, *J. Phys. Oceanogr.*, *41*(6), 1182–1208, doi:10.1175/2010JPO4564.1, 2011.

Weijer, W., M. E. Maltrud, M. W. Hecht, H. A. Dijkstra, and M. A. Kliphuis, Response of the Atlantic Ocean circulation to Greenland Ice Sheet melting in a strongly-eddying ocean model, *Geophys. Res. Lett.*, *39*(9), L09,606, doi:10.1029/2012GL051611, 2012.

Williams, K. D., et al., The Met Office Global Coupled model 2.0 (GC2) configuration, *Geosci. Model Dev.*, *8*(5), 1509–1524, doi:10.5194/gmd-88-1509-2015, 2015.

Yeager, S., and G. Danabasoglu, Sensitivity of Atlantic Meridional Overturning Circulation variability to parameterized Nordic Sea overflows in CCSM4, *J. Clim.*, *25*(6), 2077–2103, doi:10.1175/JCLI-D-11-00149.1, 2012.

Zantopp, R., J. Fischer, M. Visbeck, and J. Karstensen, From interannual to decadal: 17 years of boundary current transports at the exit of the Labrador Sea, *J. Geophys. Res. Ocean.*, *122*(3), 1724–1748, doi:10.1002/2016JC012271, 2017.

Zhang, J., Z. Liu, E. C. Brady, D. W. Oppo, P. U. Clark, A. Jahn, S. A. Marcott, and K. Lindsay, Asynchronous warming and δ¹⁸O evolution of deep Atlantic water masses during the last deglaciation, *Proc. Natl. Acad. Sci.*, *114*(42), 11,075–11,080, doi:10.1073/pnas.1704512114, 2017.

Zou, S., and M. S. Lozier, Breaking the linkage between Labrador Sea water production and its advective export to the subtropical gyre, *J. Phys. Oceanogr.*, *46*(7), 2169–2182, doi:10.1175/JPO-D-15-0210.1, 2016.